RSC Advances

PAPER

View Article Online
View Journal | View Issue

Check for updates

Cite this: *RSC Adv.*, 2023, **13**, 23285

Identification of new theobromine-based derivatives as potent VEGFR-2 inhibitors: design, semi-synthesis, biological evaluation, and *in silico* studies†

Ibrahim H. Eissa, *[a] Reda G. Yousef,[a] Hazem Elkady, [a] Eslam B. Elkaeed, [b] Aisha A. Alsfouk,[c] Dalal Z. Husein,[d] Ibrahim M. Ibrahim,[e] Mostafa A. Elhendawy,[fg] Murrell Godfrey[f] and Ahmed M. Metwaly *[hi]

Received 14th June 2023
Accepted 27th July 2023

DOI: 10.1039/d3ra04007k

rsc.li/rsc-advances

This study aimed to design anticancer theobromine derivatives inhibiting VEGFR-2. The new compounds were tested *in vitro* to evaluate their effectiveness against MCF-7 and HepG2 cancer cell lines. Among these compounds, **15a** showed the highest cytotoxicity against HepG2, with an IC_{50} value of 0.76 μM, and significant anti-proliferative effects on MCF-7, with an IC_{50} value of 1.08 μM. Notably, the selectivity index of **15a** against the two cancer cells was 98.97 and 69.64, respectively. Moreover, **15a** demonstrated potent VEGFR-2 inhibitory activity ($IC_{50} = 0.239$ μM). Further investigations revealed that **15a** induced apoptosis in HepG2 cells, significantly increasing early-stage and late-stage apoptosis percentages from 3.06% and 0.71% to 29.49% and 9.63%, respectively. It also upregulated caspase-3 and caspase-9 levels by 3.45-fold and 2.37-fold, respectively compared to control HepG2 cells. Additionally, **15a** inhibited the migration and wound healing ability of HepG2 cells. Molecular docking confirmed the binding affinities of the semi-synthesized compounds to VEGFR-2, consistent with *in vitro* results. Several computational analyses (DFT, MD simulations, MM-GBSA, PLIP, and essential dynamics) supported the stability of the **15a**-VEGFR-2 complex. Overall, the biological and computational findings suggest that compound **15a** could be a promising lead compound for the development of a novel apoptotic anticancer agent.

1. Introduction

Despite the discovery of a vast array of anticancer drugs, cancer incidence, and prevalence continue to rise significantly.[1] Developing targeted chemotherapeutic agents that can interact effectively with the molecular targets of cancer cells to inhibit their growth remains a major challenge for cancer researchers.[2] This task gives hope to developing precise lead compounds that can selectively target cancer cells while minimizing harm to healthy tissues.[3–5]

The vascular endothelial growth factor receptor-2 (VEGFR-2) is one of the most promising targets for cancer therapy. As a type of tyrosine kinase receptor, VEGFR-2 plays a crucial role in various cellular processes such as cell proliferation, adhesion, division, and angiogenesis.[6] VEGFR-2 is usually expressed much more in cancer cells than in normal cells, providing an opportunity to develop drugs that selectively target angiogenesis in tumor cells while sparing normal cells.[7]

Throughout human history, nature has been a vital source of essential resources, including medicine, food, and cosmetics.[8,9] Between the years 1981 and 2014, nearly one-

---

[a] *Pharmaceutical Medicinal Chemistry & Drug Design Department, Faculty of Pharmacy (Boys), Al-Azhar University, Cairo11884, Egypt. E-mail: Ibrahimeissa@azhar.edu.eg*

[b] *Department of Pharmaceutical Sciences, College of Pharmacy, AlMaarefa University, Riyadh 13713, Saudi Arabia*

[c] *Department of Pharmaceutical Sciences, College of Pharmacy, Princess Nourah bint Abdulrahman University, P.O. Box 84428, Riyadh 11671, Saudi Arabia*

[d] *Chemistry Department, Faculty of Science, New Valley University, El-Kharja 72511, Egypt*

[e] *Biophysics Department, Faculty of Science, Cairo University, Cairo 12613, Egypt*

[f] *Department of Chemistry and Biochemistry, University of Mississippi, University, MS 38677, USA*

[g] *Department of Agriculture Chemistry, Faculty of Agriculture, Damietta University, Damietta, Egypt*

[h] *Pharmacognosy and Medicinal Plants Department, Faculty of Pharmacy (Boys), Al-Azhar University, Cairo 11884, Egypt. E-mail: ametwaly@azhar.edu.eg*

[i] *Biopharmaceutical Products Research Department, Genetic Engineering and Biotechnology Research Institute, City of Scientific Research and Technological Applications (SRTA-City), Alexandria, Egypt*

† Electronic supplementary information (ESI) available. See DOI: https://doi.org/10.1039/d3ra04007k

third of all drugs approved by the FDA were either based on or derived from natural sources.[10] The utilization of semi-synthesis techniques on natural products enables the production of diverse analogs, leading to the discovery of more potent drugs and the repurposing of existing ones.[11] This approach also facilitates the investigation of the structure–activity relationship, which is often easier and more accessible in natural product-based drug discovery, providing a great opportunity for obtaining novel bioactive compounds, improving drug-likeness, and enhancing pharmacokinetic and pharmacodynamic properties.[12]

Theobromine, a naturally occurring alkaloid, has emerged as a promising candidate for the treatment of cancer, with evidence from both *in vitro* and *in vivo* studies suggesting its potential therapeutic value. Specifically, theobromine has been found to induce apoptosis in colorectal cancer cells,[13] and to inhibit DNA synthesis and hinder the growth of glioblastoma multiform cells.[14] Furthermore, theobromine has demonstrated anti-angiogenic

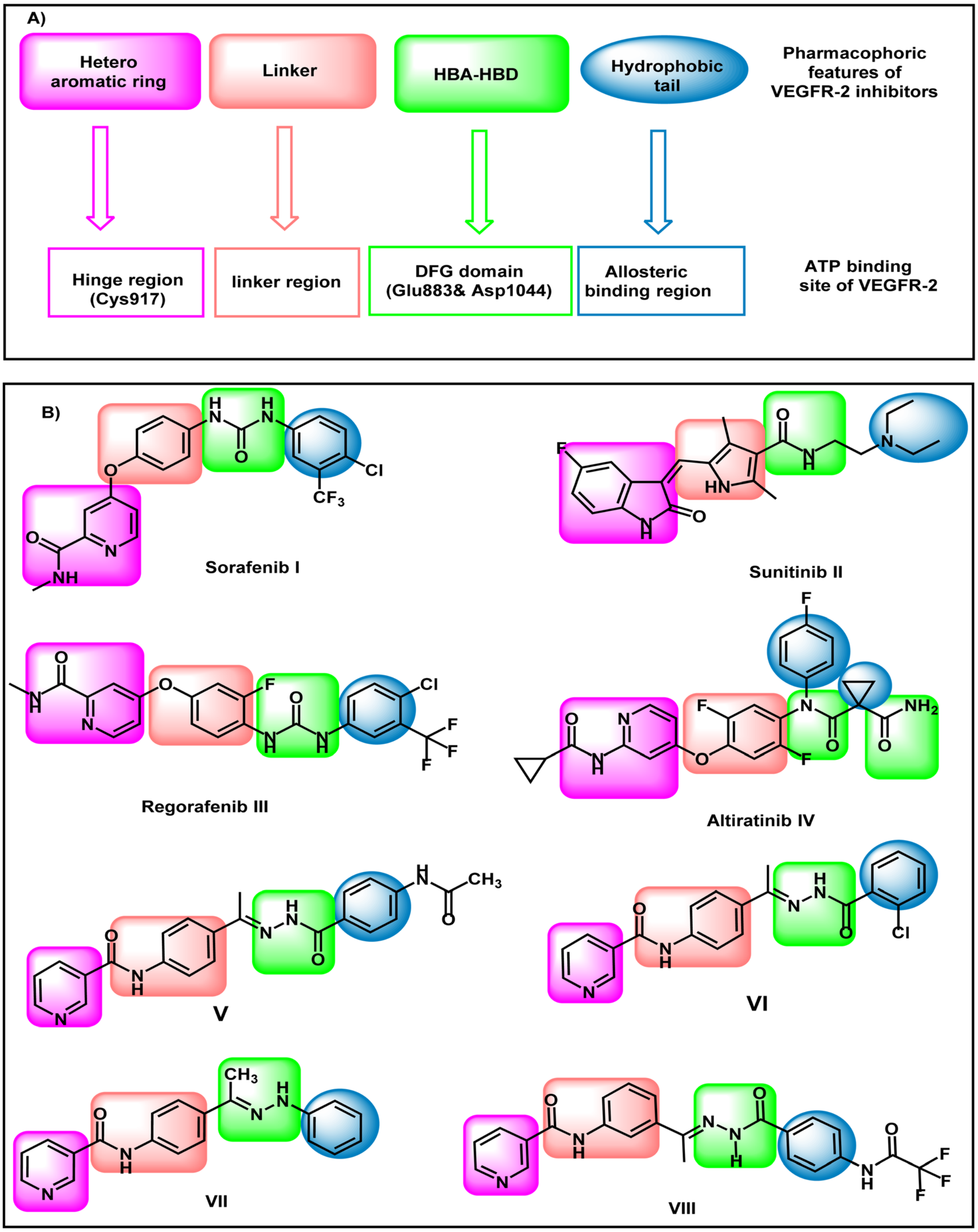

Fig. 1 (A) Pharmacophoric requirements for VEGFR-2 inhibitors. (B) Reported VEGFR-2 inhibitors.

properties by suppressing vascular endothelial growth factor (VEGF) in ovarian[15] and lung[16] cancers, indicating its potential to serve as a potent therapeutic agent against several malignancies.

2. Rationale

VEGFR-2 inhibitors have four pharmacophoric features that are crucial for the correct binding in the active site of VEGFR-2 (Fig. 1). Hetero aromatic system, linker group, pharmacophore moiety, and hydrophobic tail are the main required features. The hetero-aromatic system exerts high fitting in the hinge region of the active site. The linker group can occupy the gatekeeper region to enable the pharmacophore moiety to be oriented into the DFG motif region. The DFG motif region has two crucial amino acids (Asp1044 and Glu833) that should be activated *via* hydrogen bonding to give maximal fitting. The pharmacophore moiety should comprise at least one hydrogen bond donor and one hydrogen bond acceptor. The hydrophobic tail has a crucial role to block the allosteric pocket of the binding site.[17–19]

Sorafenib **I**,[20] sunitinib **II**,[21] regorafenib **III**, and altiratinib **IV** are reported VEGFR-2 inhibitors possessing the main pharmacophoric features. Sorafenib **I**, regorafenib **III**, and altiratinib **IV** have a pyridine moiety as a hetero-aromatic system. On the other hand, sunitinib **II** has isatin moiety as a hetero-aromatic system (Fig. 1).

Our research group has discovered compounds **V**,[22] **VI**,[22] **VII**,[23] and **VIII**[24] as potential VEGFR-2 inhibitors having promising anti-proliferative activities (Fig. 1). Such compounds possess a pyridine system to occupy the hinge region VEGFR-2. Compounds **V**, **VI**, and **VII** have a para-di-substituted phenyl ring as a linker group while compound **VIII** has a meta-di-substituted ring. Compounds **V**, **VI**, and **VIII** have a formyl hydrazone moiety as a pharmacophore system while compound **VII** possesses a hydrazone moiety. Furthermore, all the discovered compounds have substituted phenyl rings as a hydrophobic tail.

In this work, the previously synthesized compounds (**V**, **VI**, **VII**, and **VIII**) were used as lead compounds for the design and synthesis of new VEGFR-2 inhibitors. As shown in Fig. 2, the

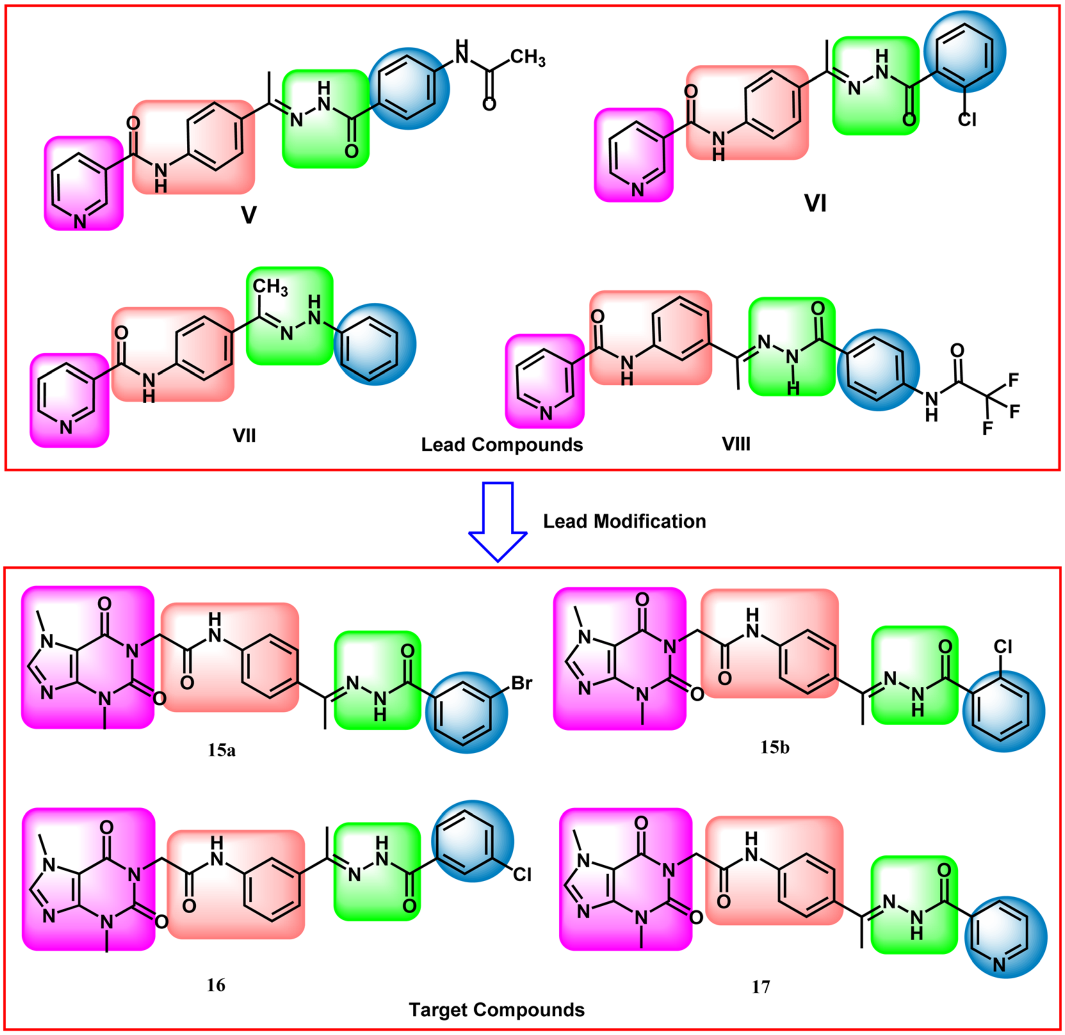

Fig. 2 Rationale design of the work.

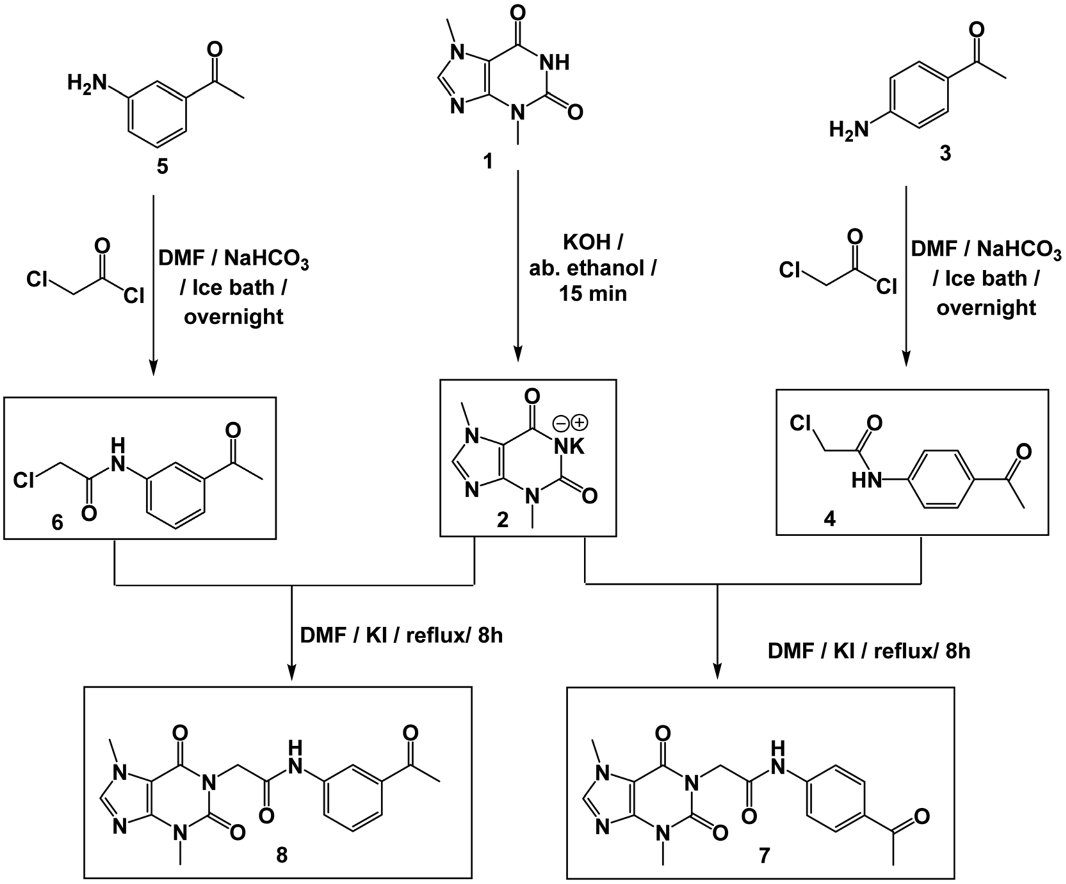

Scheme 1 Synthesis of the key intermediates **7** and **8**.

newly designed compounds have a xanthine moiety as a bioisostere for the pyridine moiety of the lead compounds. The xanthine moiety was selected for some consideration. (i) It has a large size, which is convenient for the hinge region of the VEGFR-2.[25] (ii) It has many hydrogen bond acceptor atoms, which may facilitate the hydrogen bonding interaction with the biological target. (iii) Its naturally derived nucleus increases its safety margin. For the linker group, some compounds were designed to have a di-para-substituted phenyl ring (compounds **15a**, **15b**, and **17**) and the other compound **16** has a meta di-

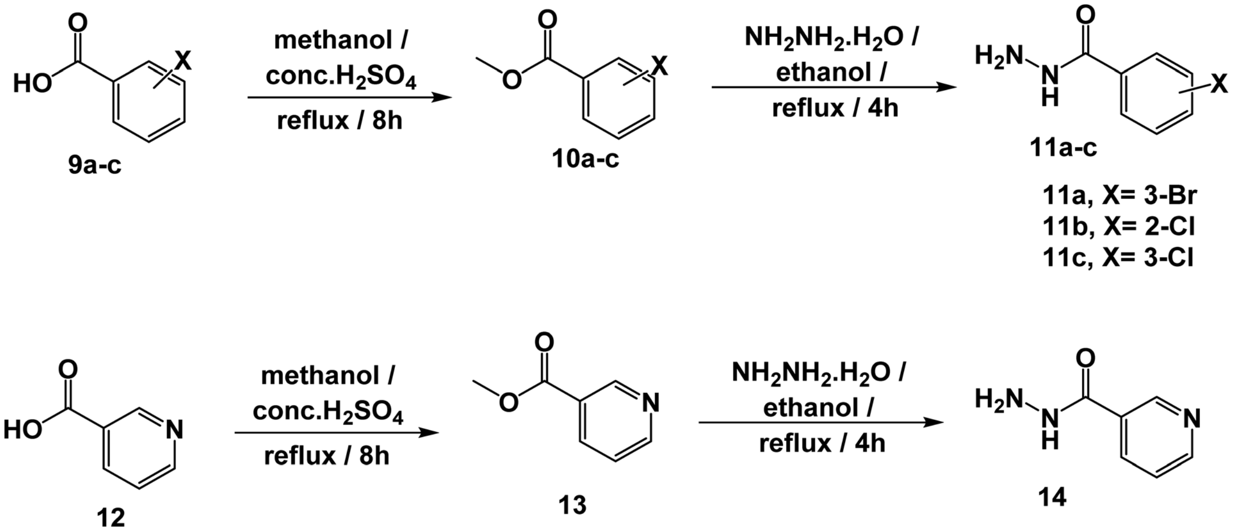

Scheme 2 Synthesis of the key intermediates **11a–d** and **14**.

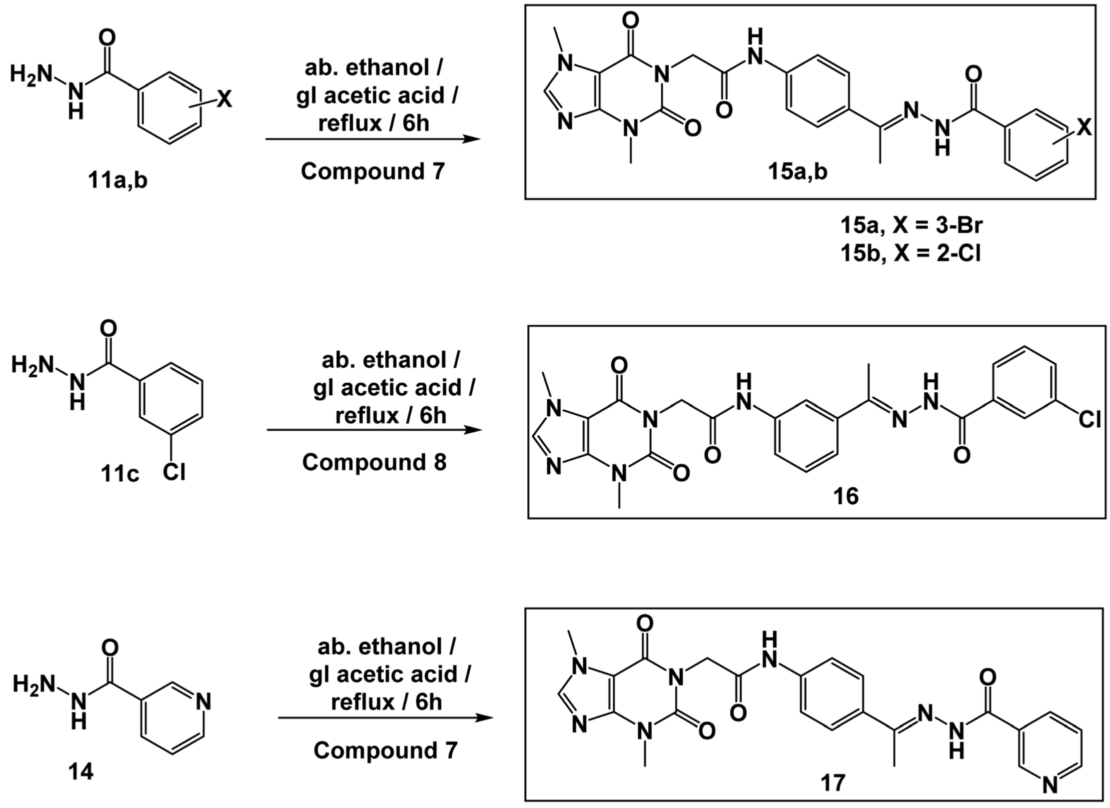

Scheme 3 Synthesis of the target compounds **15a,b**, **16**, and **17**.

substituted phenyl ring. For the pharmacophore moiety, all the designed compounds have a formyl hydrazone moiety as a pharmacophore system. Finally, different substituted phenyl rings were used as a hydrophobic tail to occupy the allosteric pocket.

3. Results

3.1. Chemistry

The synthetic pathways for the final target compounds **15a,b**, **16**, and **17** are summarized in Schemes 1, 2, and 3. Theobromine, **1**, was first converted to its potassium salt **2** by refluxing it with alcoholic KOH. *N*-(3-Acetylphenyl)-2-chloroacetamide **4** and *N*-(4-acetylphenyl)-2-chloroacetamide **6** were produced by the reaction of *p*-aminoacetophenone **3** and *m*-aminoacetophenone **5**, respectively with chloroacetylchloride in DMF using $NaHCO_3$ as a base. Equimolar amounts of theobromine potassium salt **2** reacted with **4** and **6** in DMF using potassium iodide as a catalyst to afford the key intermediates compound **7** and **8**, respectively (Scheme 1).

Moreover, benzohydrazide derivatives **11a–d** and **14** were readily prepared by refluxing the appropriate benzoate derivatives **10a–c** and **13**, respectively with hydrazine hydrate in absolute ethanol (Scheme 2).

Condensation of compound **7** with benzohydrazide derivatives **11a,b**, afforded the final target compounds **15a,b**. On the other hand, condensation of compound **8** with **11c** afforded the final target derivative **16**. Additionally, the condensation of compound **7** with **14** produced the final target compound **17** (Scheme 3).

The IR spectra of compounds **15a,b**, **16**, and **17** exhibited the appearance of absorption bands at the ranges of 3196–3265 cm^{-1} and 1667–1704 cm^{-1} attributable to the NH and C=O groups, respectively. ^1H NMR spectra of compounds **15a,b**, **16**, and **17** showed the appearance of the two amidic protons at δ ranges of 10.89–10.93 ppm and 10.42–10.45 ppm. Moreover, their ^1H NMR spectra revealed the presence of shielded singlet signals for the methyl protons at a δ range of 2.29–2.36 ppm, and singlet signals around δ 4.70 ppm for the methylene protons. In addition, ^{13}C NMR spectra showed the presence of four shielded signals at around 43.94, 33.68, 29.93, and 14.85 ppm attributed to the methylene carbon and the three-methyl carbons, respectively. Moreover, the carbonyl carbons were displayed at their expected regions.

3.2. Biology

3.2.1. *In vitro* cytotoxicity and safety. The current study used the MTT assay utilizing sorafenib as a positive control to assess the anti-proliferative effects of the synthesized derivatives **15a,b**, **16**, and **17** against HepG2 and MCF-7 cell lines. Interestingly, as summarized in Table 1, all compounds exhibited stronger IC_{50} values than those of sorafenib (2.24 ± 0.06, 3.17 ± 0.01, against HepG2 and MCF-7 cell lines, respectively). Compound **15a** was the strongest cytotoxic

Table 1 *In vitro* anti-proliferative assessment of the target compounds **15a**,**b**, **16**, and **17**

Comp.	Structure	*In vitro* cytotoxicity IC_{50} (μM)[a] HepG2	MCF-7
15a	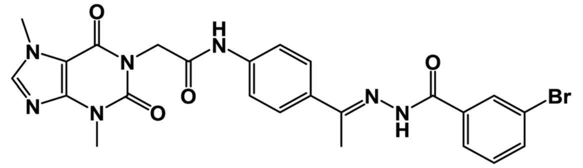	0.76 ± 0.01	1.08 ± 0.02
15b	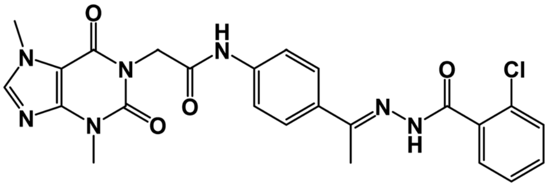	0.78 ± 0.02	0.65 ± 0.01
16	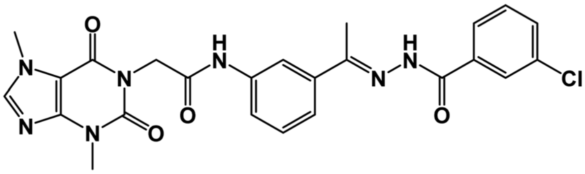	1.23 ± 0.03	2.47 ± 0.04
17	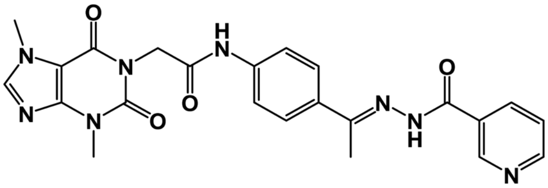	1.05 ± 0.01	0.8 ± 0.01
Sorafenib	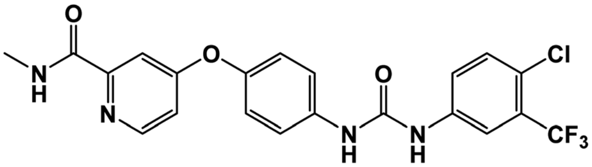	2.24 ± 0.06	3.17 ± 0.01

[a] The data were presented as the mean of three experiments.

member against HepG2 with an IC_{50} value of 0.76 ± 0.01 μM. Also, it demonstrated notable cytotoxicity against MCF-7 cells with an IC_{50} value of 1.08 ± 0.02 μM. Additionally, compounds **15b**, **16**, and **17** demonstrated considerable cytotoxic action against the same cancer cell line with IC_{50} values of 0.78 ± 0.02, 1.23 ± 0.03 μM, and 1.05 ± 0.01 μM, respectively. Also, compounds **15b** and **17** displayed strong cytotoxic action against MCF-7 cells with an IC_{50} value of 0.65 ± 0.01 μM and

Table 2 Effect of compound **15a** on stages of the cell death process in HepG2 cells

Comp.	Apoptosis Total	Early	Late	Necrosis
Compound **15a**/HepG2	29.49	9.63	12.17	7.69
Cont. HepG2	3.06	0.71	0.13	2.22

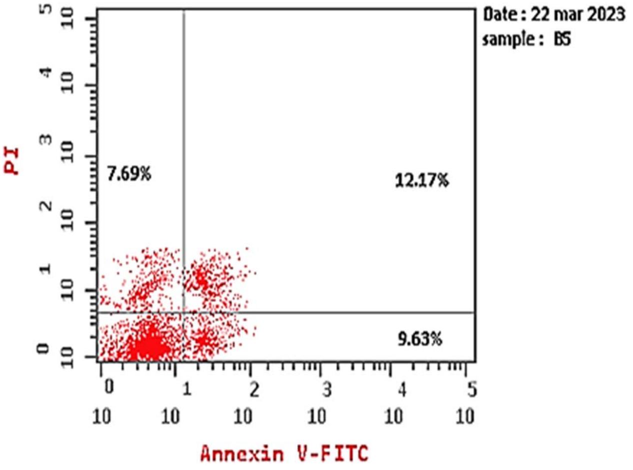

Fig. 3 Flow cytometry chart of apoptosis in HepG2 cells exposed to compound **15a**.

Table 3 Effect of compound **15a** on the levels of active caspases-3, and active caspases-9

	Protein expression	
Sample	Caspase-3	Caspase-9
Cont. HepG2	1	1
Compound **15a**/ HepG2	3.451	2.378

0.8 ± 0.01 μM, respectively. Additionally, compound **16** demonstrated a notable cytotoxicity against the MCF-7 cells with an IC_{50} value of 2.47 ± 0.04 μM.

Next, the safety of compound **15a** against Vero cells was examined to determine its selectivity against cancer cells. Based on the IC_{50} value of 75.22 μM, the selectivity index values of compound **15a** against HepG2 and MCF7 cell lines were calculated to be 98.97 and 69.64, respectively. Overall, our results imply that compound **15a** has a promising future as a secure anticancer drug and call for additional research.

3.2.2. *In vitro* VEGFR-2 enzyme assay inhibition. From the cytotoxicity results, it was concluded that compound **15a** was the strongest cytotoxic member against HepG2 (the most sensitive cancer cell line). Therefore, compound **15a** was assessed for its *in vitro* VEGFR-2 inhibitory activity using sorafenib as a reference. The results showed that compound **15a** has potent VEGFR-2 inhibitory activity with an IC_{50} value of 0.239 μM against 0.056 μM for sorafenib. These intriguing findings gave us further motivation to investigate compound **15a** 's cellular mechanistic studies.

3.2.3. Apoptosis assay. To examine the apoptotic effects of compound **15a** on HepG2 cells, a flow cytometry technique was applied. The test utilizes the Annexin V and PI double staining. According to Table 2 and Fig. 3, compound **15a** significantly increased the proportion of HepG2 cells from 3.06% to 29.49% in the early-stage apoptosis and from 0.71% to 9.63% in the late-stage apoptosis. These results imply that compound **15a** has the

Table 4 The effect of compound **15a** on HepG2's migration and healing after 48 hours

	At 0 h		At 48 h				
	Area	Width	Area	Width	RM (μm)	Wound closure (% μm^2)	Area difference (%)
Cont. HepG2	1000.333	999.3853	340.5	339.5385	13.74681	65.96135	659.8333
Compound **15a**/HepG2	1000.667	999.7462	658.6667	657.7792	7.124313	34.17722	342

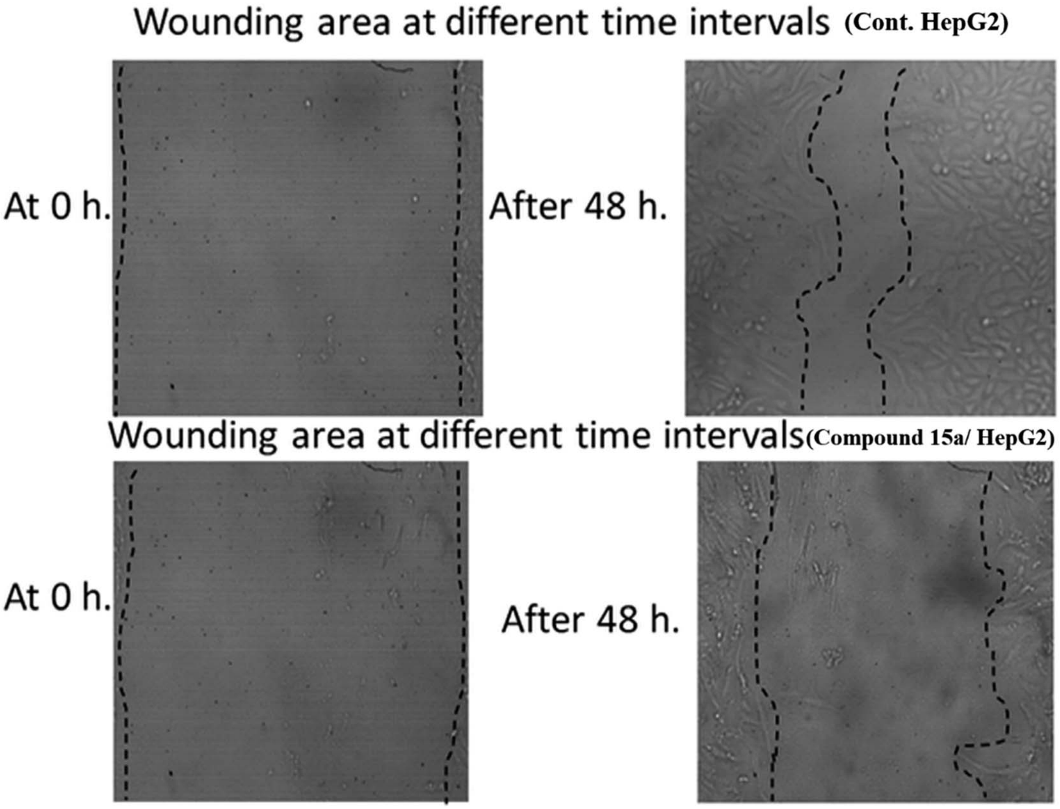

Fig. 4 The effect of compound **15a** on HepG2's migration and healing after 48 hours.

Table 5 The binding energies (ΔG) of the theobromine derivatives and sorafenib against VEGFR-2

Comp.	**15a**	**15b**	**16**	**17**	Sorafenib
ΔG [kcal mol^{-1}]	−23.29	−24.74	−23.09	−23.11	−21.20

potential to be cytotoxic and may be linked to programmed cell death in the HepG2 cells.

3.2.4. Effects on caspases. This study examined the effects of compound **15a** at a concentration of 0.76 μM (IC_{50} value) on the expression levels of caspase-3 and caspase-9 in HepG2 cells. In comparison to the control, the results showed that compound **15a** increased the level of caspase-3 by 3.45-fold, compared to the control. Furthermore, compound **15a** exhibited a significant increase in the level of caspase-9 by 2.37-fold, compared to the control (Table 3).

3.2.5. The effect of compound 15a on HepG2's migration and healing. To assess the impact of compound **15a** on the migration and healing of HepG2 cancer cells, a wound healing assay was applied. This technique involves making a scratch on a cancer cell monolayer, measuring the initial diameter, and monitoring the closure of the scratch at specific time intervals for both treated and untreated cells. The images of the scratch areas of treated and untreated cell lines were compared after 0 and 48 hours. The results (shown in Table 4 and Fig. 4) indicated that the scratch of the untreated HepG2 cells closed significantly within 48 hours, reducing the width by 65.9%. On

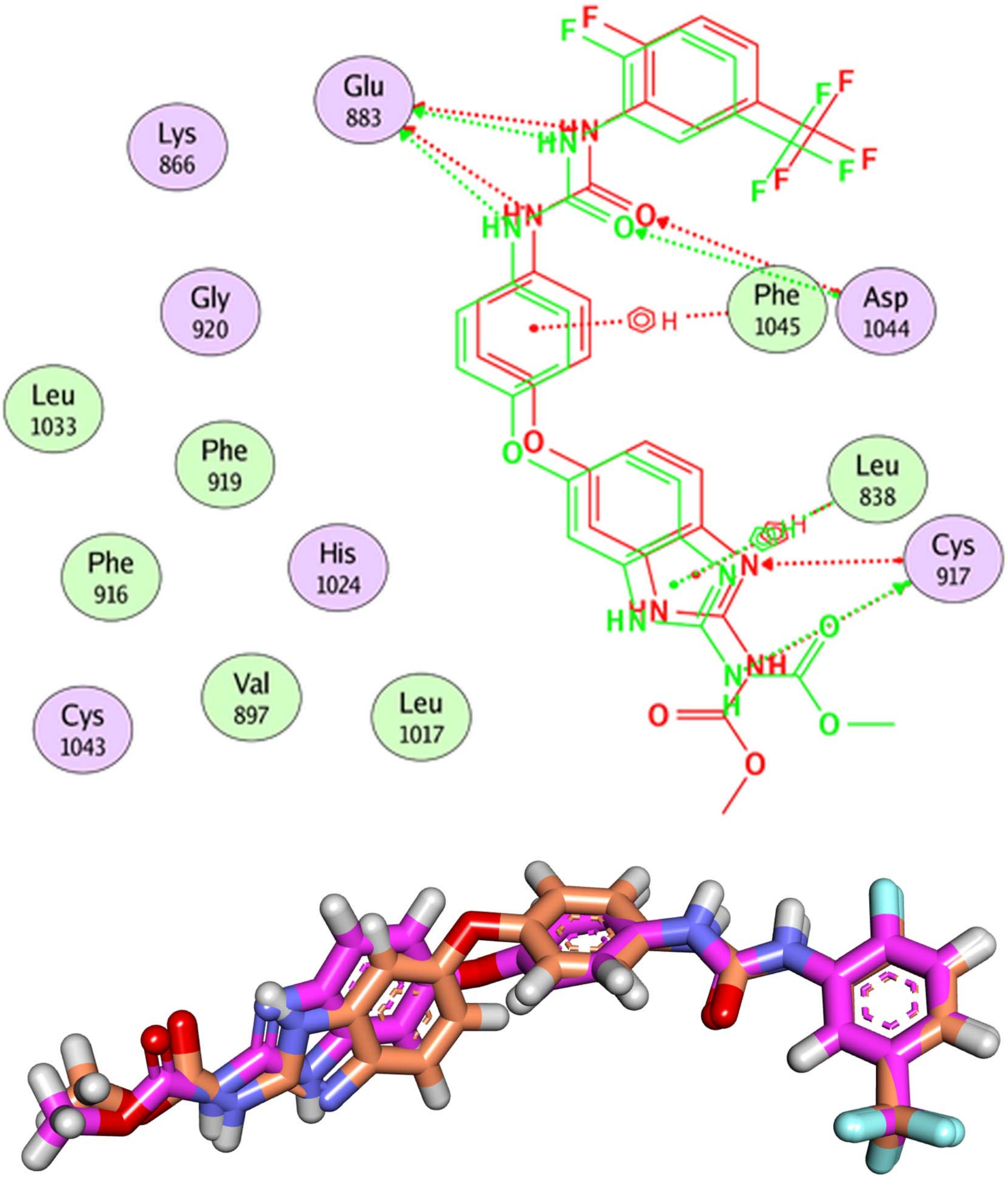

Fig. 5 Validation of the docking process. The RMSD value between the original ligand (pink) and the docked one (orange) is 1.19 Å.

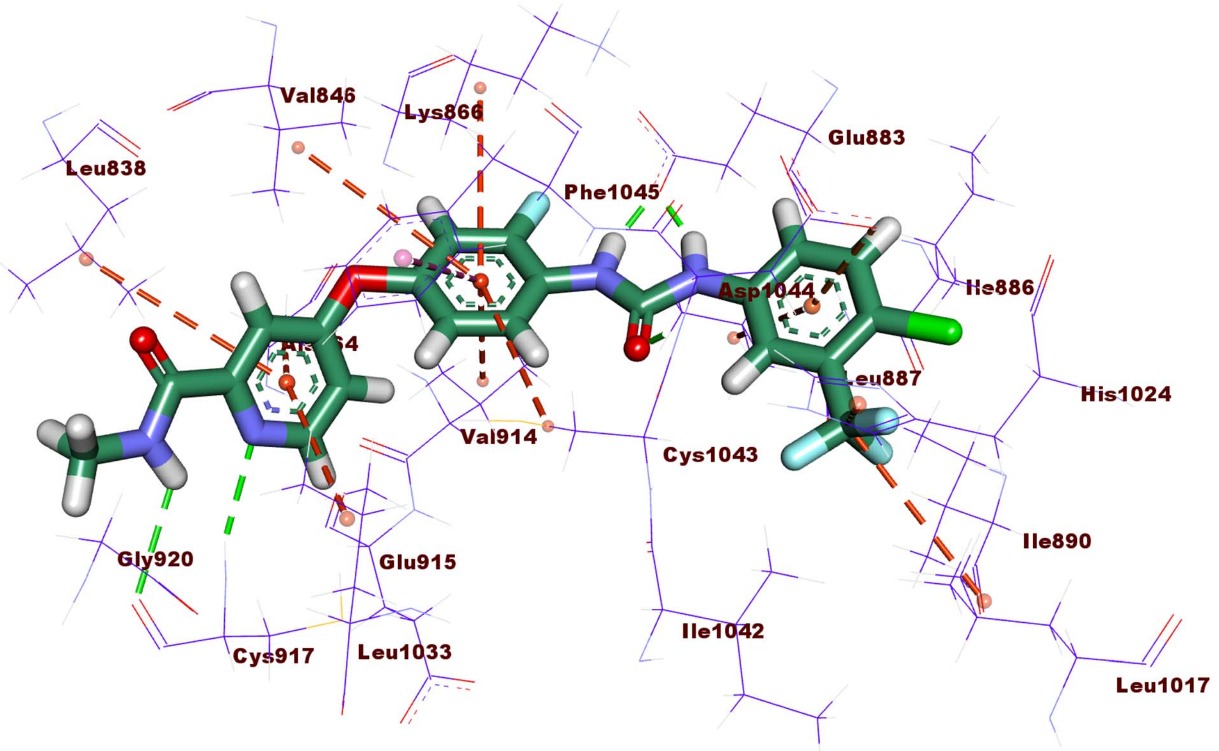

Fig. 6 2D interaction of sorafenib with the active site of VEGFR-2.

the other hand, the scratch width of HepG2 cells treated with compound **15a** decreased by only 34.17%, indicating that the treatment significantly inhibited the closure of the scratch.

3.3. Computational studies

3.3.1. Molecular docking. The crystal structure of VEGFR-2 (PDB ID: 2OH4) was downloaded from the protein data bank and prepared for docking using MOE2019 software and sorafenib as a reference molecule. The binding pattern of the synthesized compounds as well as sorafenib were clarified in the following figures. The binding energies (ΔG) of the tested compounds were summarized in Table 5.

At first, the validation process was carried out by docking the co-crystallized ligand in the active pocket of VEGFR-2. The co-crystallized ligand has a general name of benzimidazole-urea inhibitor. In addition it has an IUPAC name of methyl *N*-[5-[4-[[2-fluoro-5-(trifluoromethyl) phenyl]carbamoylamino] phenoxy]-1-methylbenzimidazol-2-yl]carbamate. The results indicated the high validity of the docking process since the RMSD value between the docked and original ligand was (1.19 Å) less than 2.00 Å (Fig. 5).

The reference molecule, sorafenib, revealed a binding mode similar to the reported results.[22–24] It had an energy score of −21.20 kcal mol^{-1}. It formed one hydrogen bond with Cys917 and three hydrophobic interactions with Leu838, Ala864, and Leu1033 at the hinge region. In addition, its linker moiety formed six hydrophobic interactions with Val914, Val846, Cys1043, and Phe1045. Furthermore, the pharmacophore moiety was engaged in three hydrogen bonds with Glu883 and Asp1044. The terminal hydrophobic tail formed five hydrophobic interactions with Leu887, Cys1043, His1024, and Leu1017. Also, it formed an electrostatic interaction with **Asp104** (Fig. 6).

Compound **15a** has a binding energy of −23.29 kcal mol^{-1}. The different features occupied the different sub-pockets of the active site. The heterocyclic system (xanthine moiety) was oriented into the hinge region forming one hydrogen bond and two hydrophobic interactions with Cys917, Leu838, and Phe916. The linker (phenyl) moiety formed one hydrophobic interaction with Val914 and one electrostatic attraction with Cys1043. The *N*-ethylideneformohydrazide moiety occupied the DFG motif region and formed two hydrogen bonds and three hydrophobic interactions with Glu883, Asp1044, Lys866, Val914, and Leu887. The terminal hydrophobic tail (3-bromophenyl moiety) occupied the allosteric pocket forming two hydrophobic interactions with Ile886 and Ile890. In addition, it formed one electrostatic interaction with Asp1044 (Fig. 7A).

Compound **15b** showed a binding score of −24.74 kcal mol^{-1}. The xanthine moiety occupied the hinge region of VEGFR-2 forming one hydrogen bond and two hydrophobic interactions with Cys917, Leu838, and Phe916. The phenyl moiety formed three hydrophobic interactions with Val914, Ala864, and Val846. In addition, it formed one electrostatic attraction with Cys1043. The *N*-ethylideneformohydrazide moiety occupied the DFG motif region forming two hydrogen bonds and three hydrophobic interactions with Glu883, Asp1044, Lys866, Val914, and Leu887. The 2-chlorophenyl moiety occupied the allosteric pocket forming five hydrophobic

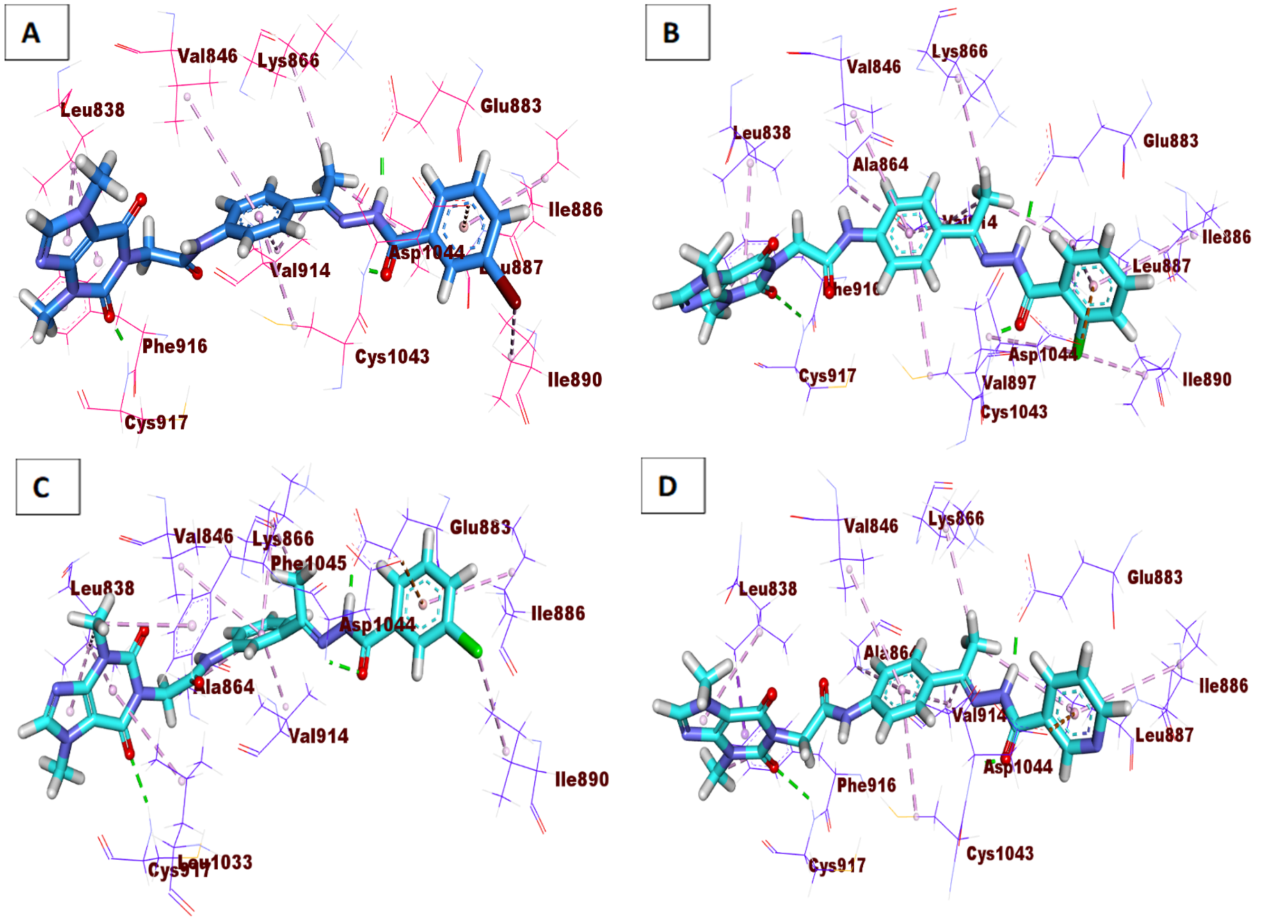

Fig. 7 3D interactions of the synthesized compounds in the VEGFR-2 binding site. (A) Compound **15a**, (B) compound **15b**, (C) compound **16**, (D) compound **17**.

Table 6 ADMET screening of the synthesized compounds

Comp.	BBB level	Solubility level	Absorption level	Hepatotoxic prediction	CYP2D6 prediction	PPB prediction
15a	Very low	Low	Moderate	Non-toxic	Non-inhibitor	<90%
15b		Good				
16		Low				
17		Good		Toxic		
Sorafenib		Very low	Good			>90%

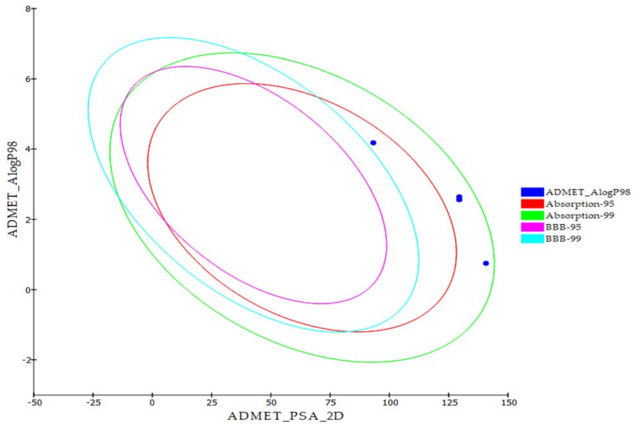

Fig. 8 The executed ADMET study.

interactions with Ile886, Val879, Leu887, and Ile890. In addition, it formed one electrostatic interaction with Asp1044 (Fig. 7B).

Compound **16** showed a binding score of -23.09 kcal mol^{-1}. The xanthine moiety formed one hydrogen bond with Cys917 and five hydrophobic interactions with Leu838, Leu1033, and Phe1045. The central phenyl moiety formed four hydrophobic interactions with Val914, Ala864, Lys866, and Val846. The *N*-ethylideneformohydrazide moiety occupied the DFG motif region forming two hydrogen bonds and one hydrophobic interaction with Glu883, Asp1044, and Lys866. The 3-chlorophenyl moiety occupied the allosteric pocket forming two hydrophobic interactions with Ile886 and Ile890. In addition, it formed one electrostatic interaction with Asp1044 (Fig. 7C).

Table 7 Toxicity study of the synthesized compounds

Comp.	Ames prediction	Rat-male-FDA	Carcinogenic potency TD_{50} (mouse)[a]	Rat oral LD_{50}[b]	Rat chronic LOAEL[b]	Skin irritancy	Ocular irritancy
15a	Non-mutagen	Non-carcinogen	23.973	1.785	0.046	Non-irritant	Mild
15b			18.268	1.580	0.108		
16			24.482	1.305	0.046		
17			27.036	0.768	0.062		
Sorafenib			19.236	0.823	0.005		

[a] Unit: mg kg^{-1} body weight per day. [b] Unit: g kg^{-1} body weight.

Compound **17** showed a binding score of −23.11 kcal mol^{-1}. The xanthine moiety was engaged in one hydrogen bond and three hydrophobic interactions with Cys917, Leu838 and Phe916. The central phenyl ring occupied the central region forming three hydrophobic interactions with Val914, Ala864, and Val846. The *N*-ethylideneformohydrazide moiety occupied the DFG motif region forming two hydrogen bonds and three hydrophobic interactions with Glu883, Asp1044, Lys866, Val914, and Leu887. The terminal pyridine moiety occupied the allosteric pocket forming two hydrophobic interactions with Ile886 and Leu887. In addition, it formed one electrostatic interaction with Asp1044 (Fig. 7D).

3.3.2. Correlation of docking studies and biological results. Sorafenib has ideal binding mode against the active site of VEGFR-2. It formed two hydrogen bonds at the hinge region with Cys917. In addition, it formed three hydrogen bonds at the DFG motif region with Asp1044 and Glu883. These hydrogen bonds give a high stability at the active site for long time. This indicates the high affinity of sorafenib with VEGFR-2 and reflects the high inhibitory activity against VEGFR-2. The tested compounds showed binding energies higher than that of sorafenib ranging from-23.09 to −24.74 kcal mol^{-1}. The higher scores of the synthesized compounds may be related to the hydrophobic interactions and van der Waals forces.

On the other hand, although compound **15a** has good binding mode against VEGFR-2, it showed number of hydrogen bond interactions less than that sorafenib. It formed one hydrogen bond ay the hinge region and two hydrogen bonds at the DFG motif region. Such results reflect the higher activity of sorafenib as VEGFR-2 (IC_{50} = 0.056 μM) than compound **15a** (IC_{50} = 0.239 μM).

Investigating the binding modes of the four synthesized compounds indicated that all of them have the same number of hydrogen bonds at the hinge region (one bond) and the DFG motif region (two bonds).

Observing the cytotoxicity of compounds **15a** and **15b** against the most sensitive cells (HepG2), these two compounds have non-significant differences with IC_{50} values of 0.76 and 0.78 μM, respectively. Such biological results match with the docking results, as these two compounds have the same number of hydrogen bonds with non-significant difference in the binding energy (ΔG = −23.29 and −24.74 kcal mol^{-1}, respectively).

Regarding compounds **16** and **17**, although these compounds have the same binding mode as compounds **15a** and **15b**, both of them have less cytotoxic activity against HepG2. The reduced activity of compound **16** may be due to the change in the configuration of the linker moiety, as this compound has a meta-disubstituted phenyl linker while compounds **15a**, **15b**, and sorafenib have a para-disubstituted phenyl linker. Moreover, the reduced activity of compound **17** may be due to the absence of halogen atoms at the hydrophobic tail in contrast to that of compounds **15a**, **15b**, and sorafenib. It is well-known that halogen atoms have a high participation in hydrophobic interaction in the active site.

3.3.3. *In silico* ADME analysis. In order to detect the ADMET parameters of the synthesized compounds, Discovery Studio 4.0 software was used. Sorafenib was used as a reference molecule. As shown in Table 6, the synthesized molecules have very low BBB penetration levels expecting the absence of CNS toxicity. For the predicted aqueous solubility, compounds **15b** and **17** showed good levels while compounds **15a** and **16** showed low levels. Regarding the expected intestinal absorption of the tested molecules, all of them showed moderate levels. The tested molecules were expected to be devoid of cytochrome P450 (CYP-2D6) inhibitory activity indicating the non-hepatotoxicity except for compound **17**. Finally, all the examined molecules were expected to bind plasma protein less than 90% (Fig. 8).

3.3.4. Toxicity studies. Additional *in silico* study was carried out for the synthesized molecules to predict their toxicity potential against different validated models in Discovery studio software. Sorafenib was used as a reference molecule. The expected toxicity results were summarized in Table 7.

At first, the mutagenic potential of a particular molecule can be assessed using the Ames prediction model. Depending on this model, all the synthesized molecules were predicted to be non-mutagenic. Furthermore, the FDA rodent carcinogenicity model can predict the carcinogenicity of a particular compound. This model indicated that the synthesized compounds are non-carcinogens. In addition, the carcinogenic potency TD_{50} values of the synthesized compounds ranged from 23.973 to 27.036 g kg^{-1}. This range of carcinogenic potency TD_{50} values was higher than that of sorafenib (19.236 g kg^{-1}) indicating the safety margin of the synthesized compounds. An additional sigh for the safety of the tested compounds was reached by the rat oral LD_{50} model. This model predicted that compounds **15a**, **15b**, and **16** have rat oral LD_{50} values ranging from 0.768 to 1.785 g kg^{-1}, which were higher than that of sorafenib (0.823 g kg^{-1}). For the rat chronic LOAEL model which predicts the rat chronic lowest observed adverse effect level value of a chemical, all compounds (0.046–0.108 g kg^{-1}) have higher values than sorafenib (0.005 g kg^{-1}). All compounds were predicted to be non-irritant with mild irritancy against the skin and the eyes, respectively (Table 7).

3.3.5. Molecular dynamic (MD) simulation. The conformation of compound **15a** and the reference compound, sorafenib, and their distance from the protein's center of mass were both stable throughout the production run. After around 20 ns, the RMSD values for apo (blue line) and VEGFR-2 & **15a** complex (red line) had equilibrated at about 2.7 Å and 4 Å, respectively. In addition, the reference compound (VEGFR-2 & sorafenib) shows more stable values around 2 Å throughout the simulation as shown by the green line (Fig. 9A). In Fig. 9B, we can see that the RMSD of **15a** (blue line) has stabilized around 4 Å while the sorafenib compound (red line) shows a more stable fluctuation with an average of around 2 Å. As can be seen in Fig. 9C, the average apo (blue line), VEGFR-2 & **15a** complex (red line), and VEGFR-2 & sorafenib complex (green line) systems show a radius of gyration with values near each other with the VEGFR-2 & sorafenib as the most stable one followed by the apo protein then the VEGFR-2 & **15a** complex. As shown in Fig. 9D, apo protein, VEGFR-2 & **15a** complex, and VEGFR-2 & sorafenib complex had average SASA values of 17 656 $Å^2$, 18 076 $Å^2$, and 17 180 $Å^2$, respectively. Fig. 9E showed that the average number of H-bonds formed between each compound and the VEGFR-2 protein differs across the two systems. The 15a compound (blue line) forms 1 H-bond during a low number of frames with zero H-bond as a common number. On the other hand, sorafenib compound (pale red line) shows that at least there is a constant 1 H-bond with 2 H-bonds as less common. Overall, this demonstrates that the protein structure is rather stable. A comparison between the three systems RMSF shows that no significant fluctuation is happening (Fig. 9F). The separation between the **15a** and the protein centers of mass is stable with an average distance of 7 Å which is slightly smaller than the distance of sorafenib 7.8 Å, indicating a stable interaction (Fig. 9G).

3.3.6. MM-GBSA studies. The MM-GBSA method's breakdown of the binding free energy into its component was shown in Fig. 10. The binding energy of compound **15a** is −36.9 kcal mol^{-1} which is slightly smaller than the reference compound by 8.5 kcal mol^{-1}, indicating a slightly weaker interaction compared to the reference. The electrostatic interactions (−3.41 kcal mol^{-1}) are less significant than the van der Waals interactions (−56.79 kcal mol^{-1}) in determining binding stability for **15a.** On the other hand, the reference compound shows a larger average electrostatic contribution (−20 kcal mol^{-1}) and slightly smaller van der Waals interactions (−52.5 kcal mol^{-1}). Using decomposition analysis, the contributions of amino acids within 1 nm of compound **15a** or sorafenib were calculated and compared (Fig. 11). Leu838

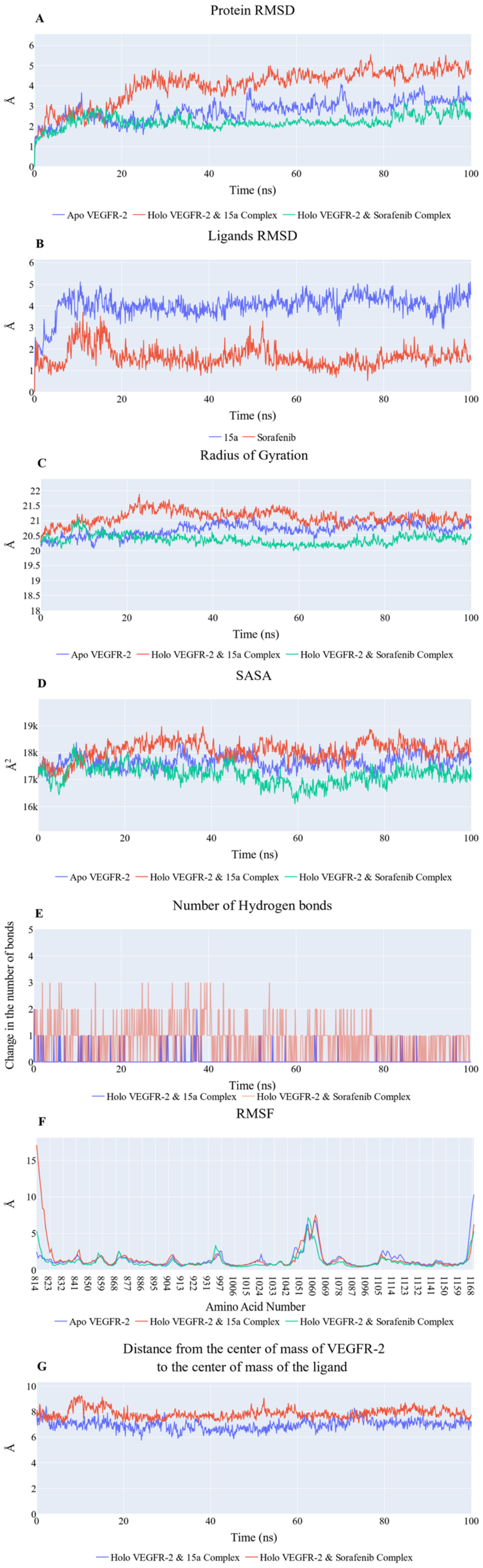

Fig. 9 (A) RMSD values from the trajectory for the VEGFR-2 protein in apo form (blue line) and holo forms (red line for **15a** system and green for sorafenib system). (B) Ligand RMSD values (**15a**: blue line, sorafenib: green line). (C) Radius of gyration for the VEGFR-2 protein in apo form (blue line) and holo forms (red line). (D) SASA for the VEGFR-2 protein in apo form (blue line) and holo forms (red line for **15a** system and green for sorafenib system). (E) Change in the number of hydrogen bonds between **15a** and VEGFR-2 protein (blue line) and sorafenib and VEGFR-2 protein (red line). (F) RMSF for the VEGFR-2 protein in apo form (blue line) and holo forms (red line for **15a** system and green for sorafenib system). (G) Distance from the center of mass of compound **15a** or sorafenib and VEGFR-2 protein.

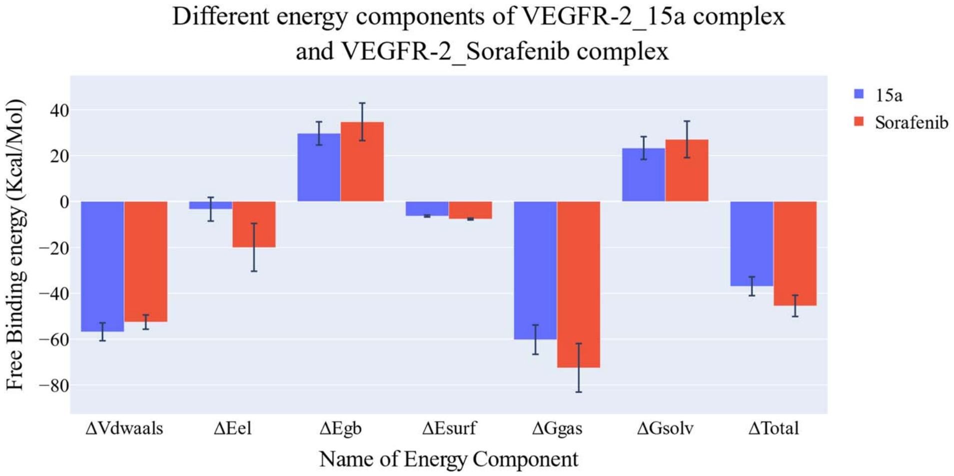

Fig. 10 Different energetic components of MM-GBSA. Bars represent the standard deviations.

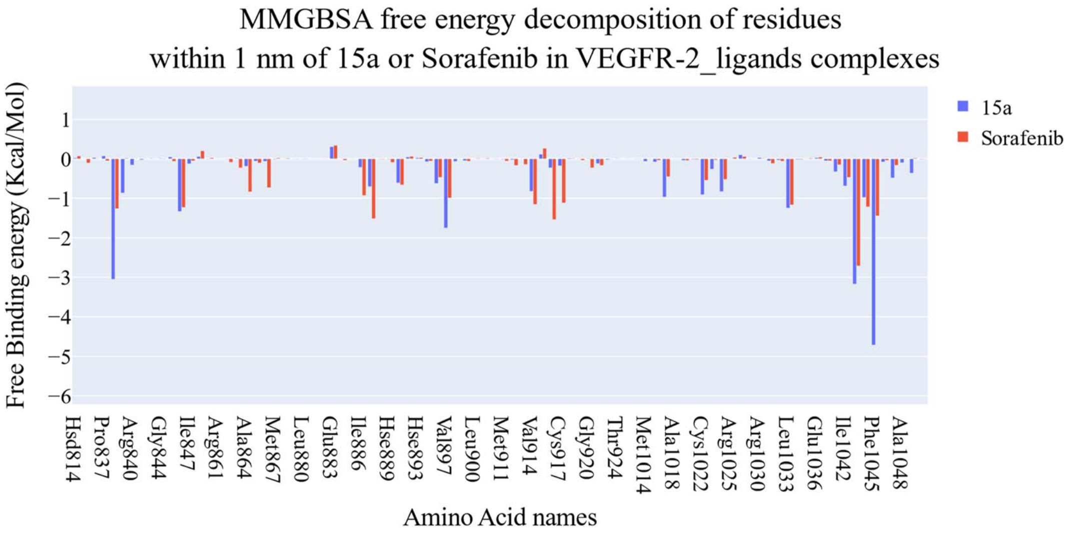

Fig. 11 Comparison between the binding free energy decomposition of the VEGFR-2_**15a** complex and VEGFR-2_sorafenib complex.

(-3.05 kcal mol^{-1} for **15a** *vs.* 1.25 kcal mol^{-1} for sorafenib), Val846 (-1.33 kcal mol^{-1} for **15a** *vs.* -1.22 kcal mol^{-1} for sorafenib), Leu887 (-0.7 kcal mol^{-1} for **15a** *vs.* -1.51 kcal mol^{-1} for sorafenib), Val897 (-1.74 kcal mol^{-1} for **15a** *vs.* -0.99 kcal mol^{-1} for sorafenib), Val914 (-0.82 kcal mol^{-1} for **15a** *vs.* -1.15 kcal mol^{-1} for sorafenib), Phe916 (-0.22 kcal mol^{-1} for **15a** *vs.* -1.53 kcal mol^{-1} for sorafenib), Cys917 (-0.17 kcal mol^{-1} for **15a** *vs.* 1.11 kcal mol^{-1} for sorafenib), Leu1033 (-1.24 kcal mol^{-1} for **15a** *vs.* -1.16 kcal mol^{-1} for sorafenib), Cys1043 (-3.17 kcal mol^{-1} for **15a** *vs.* -2.71 kcal mol^{-1} for sorafenib), Asp1044 (-0.98 kcal mol^{-1} for **15a** *vs.* -1.21 kcal mol^{-1} for sorafenib), and Phe1045 (-4.71 kcal mol^{-1} for **15a** *vs.* -1.43 kcal mol^{-1} for sorafenib) are the amino acids that have a contribution less than -1 kcal mol^{-1}.

Extremely long-lasting hydrophobic interactions (90.2% occurrence or greater) are present between compound **15a** and Leu838, Val846, Leu887, Val897, Leu1017, Cys1022, His1024, Leu1033, Cys1043, Asp1044, and Phe1045 amino acids (Fig. 12A–C). Phe1045 also often formed Pi-stacking, with a rate of 90.6%. Out of these amino acids, Leu838, Val846, Val897, Leu1033, Cys1043, and Phe1045 show a good contribution to the binding energy and high incidence. Comparing these amino acids with the interacting amino acids from docking, we can see that Leu838, Val846, and Cys1043 remained in contact with the **15a** compound for more than 90% of the time and showed a good contribution of the binding. After clustering, PLIP was used to extract 3D binding interactions as .pse files using representative frames (Fig. 13). Similarly, the reference compound shows that there are 15 amino acids (Leu838, Val846, Ala864, Lys866, Ile886, Leu887, Ile890, Val897, Val914, Leu1017, His1024, Leu1033, Cys1043, Asp1044, and Phe1045) that interact with sorafenib compound using hydrophobic interaction with a proportion of at least 90%. In addition, Asp1044 was found to form a H-bond with a proportion of 81.3% and Phe1045 forms a Pi-stacking of 83% (Fig. 14A–C).

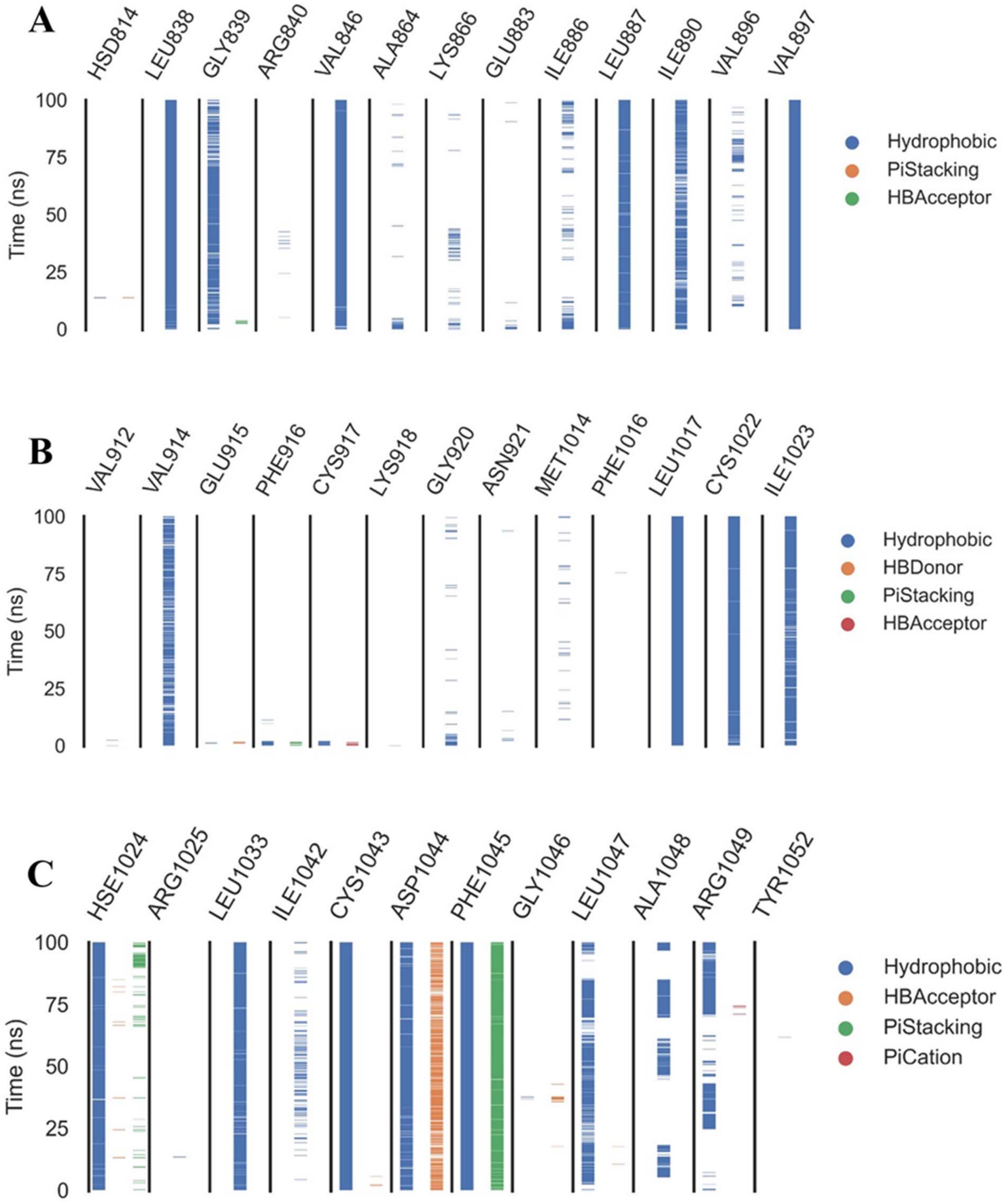

Fig. 12 The amino acids, the types of interactions with **15a**, and their occurrence during the whole simulation time using the ProLIF python library. (A) Amino acids panel from HSD814 to VAL897, (B) amino acids panel from VAL912 to ILE1023 and (C) amino acids panel from HES1024 to TYR1052.

Leu838, Val846, Leu887, Val914, Leu1033, Cys1043, Asp1044, and Phe1045 are the amino acids that show high persistence and high contribution to the binding energy. Out of the most common amino acids, Val846, Ala864, Leu887, Val914, Leu1017, Leu1033, Cys1043, and Asp1044 remained in contact with the sorafenib from docking. The representative frames obtained from clustering each trajectory were used with PLIP to identify the interactions and get the 3D binding conformation as .pse files (Fig. 15).

3.3.7. Principle component analysis (PCA).

With the use of PCA, the trajectory's high-amplitude, and coordinated motion was identified. As mentioned in the methods section, we used

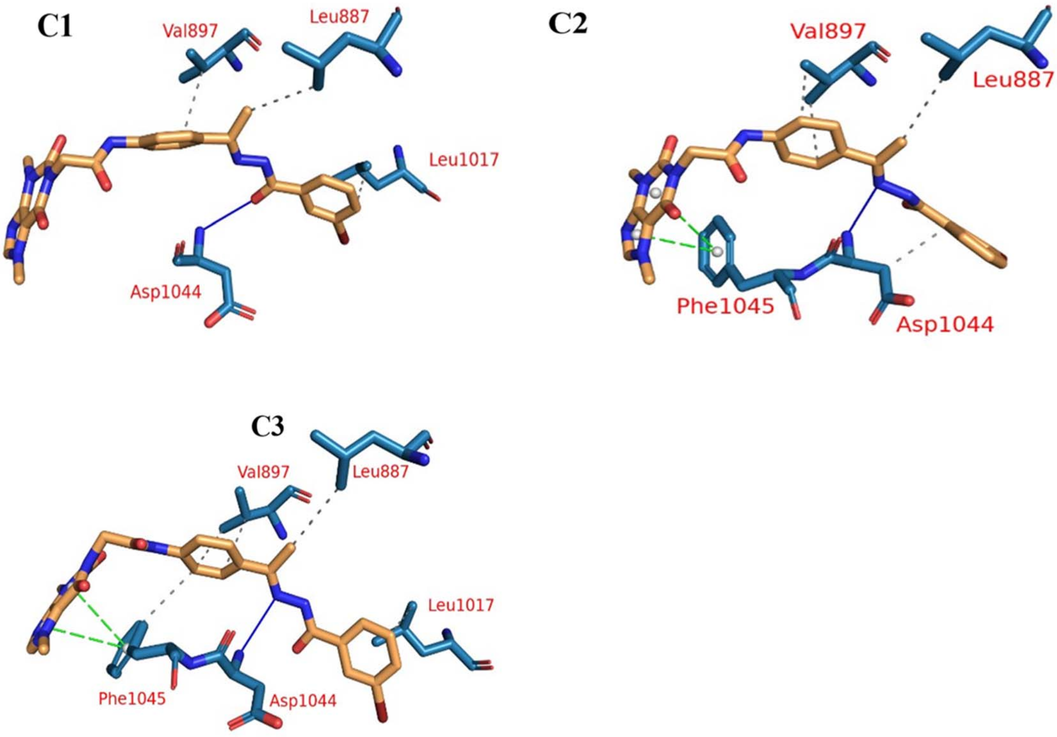

Fig. 13 The three clusters representative obtained from TTClust and their 3D interactions with **15a**. Grey dashed lines: hydrophobic interactions, blue solid lines: H-bonds, green dashed line: Pi-stacking interaction, orange sticks: **15a**, blue sticks: amino acids of VEGFR-2 protein.

the scree plot to determine the number of PCs that contains large variance. We can see that the slope at the 2nd PC showed a large decrease. Moreover, 81.8% of the entire variance was accounted for by the first eigenvector alone, and almost 89.5% of the total variance was accounted for by the first three eigenvectors (Fig. 16).

3.3.8. Bi-dimensional projection calculations. In Fig. 17, 18, 19, we see the results of projecting each trajectory onto the first three eigenvectors of the combined C matrix. The bigger marker in these figures represents the average structure of the trajectories. Fig. 17 (a projection on the first two eigenvectors) demonstrated how the two trajectories differ in their average structure and showed sampling that rarely coincides. Fig. 18 showed that the two average structures projected onto the first and third eigenvectors still seem distinct, but the overlap between the two trajectories was much larger. Finally, projection on the second and third eigenvectors (Fig. 19) revealed that the two trajectories are quite dissimilar and have minimal overlap. The motion associated with the first three eigenvectors was shown using porcupine diagrams (Fig. 20). The Gly1046:-Leu1065 loop was the biggest motion represented by these three eigenvectors. The first eigenvector of both trajectories describes the same motion (loop opening). The second eigenvector indicated that the loop opens in the green apo structure with a loop rotation while it closes in the red holo structure. The movement captured for the apo protein in the third eigenvector showed the loop opening as the protein becomes more compact, whereas the motion captured for the holo protein showed just the loop closing.

3.3.9. DFT calculations. After optimizing the neutral singlet molecular structure under DFT/B3LYP/6-311++G(d,p) theory level, the charge distribution function was analyzed using Mulliken analysis. The labeled chemical system of **15a** includes 282 electrons and 58 atoms as shown in the labeled molecular scheme, Fig. 21a. The outcomes of the Mulliken population study of compound **15a** at DFT-B3LYP/6-311G++(d,p) level, which was used to determine the atomic charge values, are displayed in Fig. 21b. All anticipated values show that the molecule under investigation has significant charge delocalization. Over the hydrogen atoms, the positive charges are concentrated and the most positively charged carbon atoms in the suggested molecule are C21 and C29, which are ready to be attacked by nucleophilic targets. The most negative carbons are C12 and C26 as demonstrated in Fig. 21b. The estimated dipole moment (D_m, 11.59Debye) in Table 8 suggested that the designed structure is reactive with high internal interaction.[26]

To shed more light on the reactivity of **15a**, frontier molecular orbital analysis has been explored. As demonstrated in Fig. 21c, HOMO is localized all over most parts of the molecule while LUMO is localized over the middle part of the structure. The energy gap value, E_{gap}, between HOMO and LUMO is 7.73 eV predicting a small energy is needed for electronic transition within the molecule. Such findings confirm the potential biological reactivity of **15a.**

The computational indices that depend on HOMO and LUMO energies such as global softness (σ), global hardness (η), chemical potential (μ), electron affinity (EA), and electrophilicity index

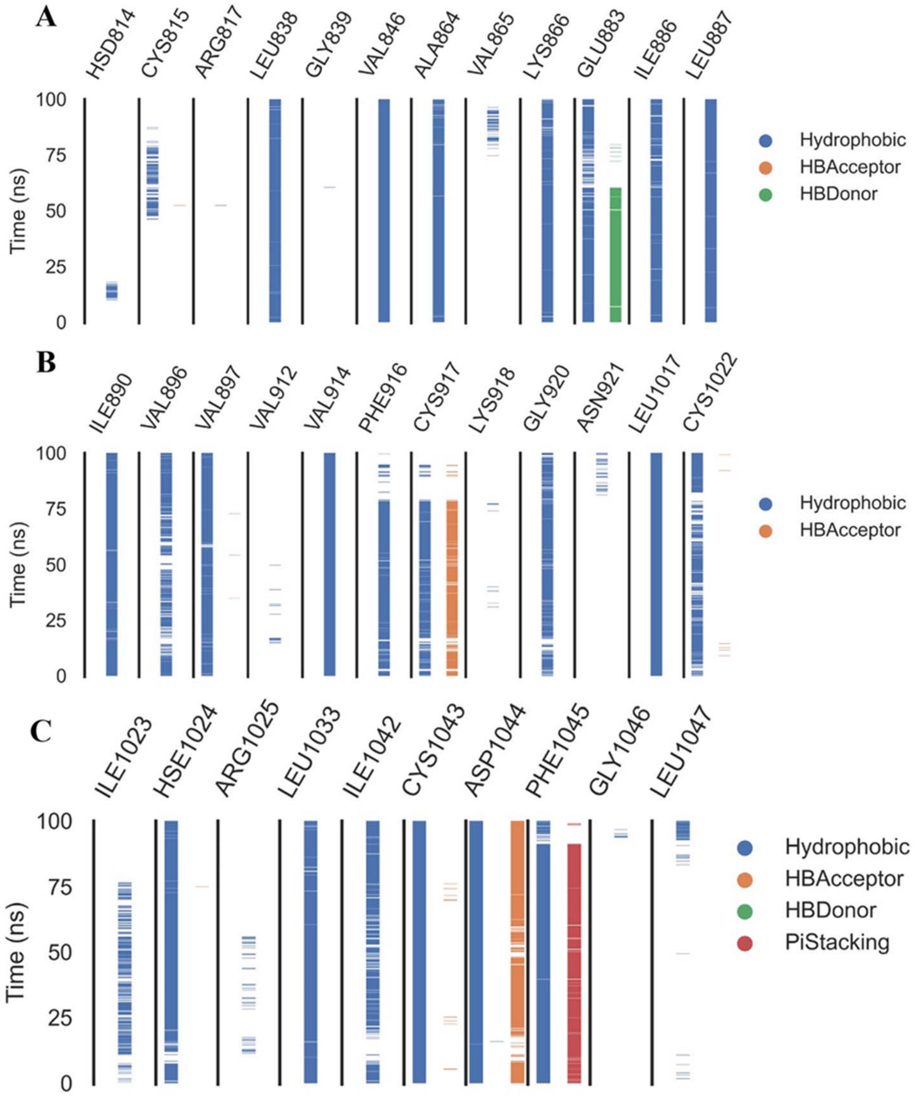

Fig. 14 The amino acids, the types of interactions with compound sorafenib, and their occurrence during the whole simulation time using the ProLIF python library. (A) Amino acids panel from HSD814 to LEU887, (B) amino acids panel from ILE890 to CYS1022 and (C) amino acids panel from ILE1023 to LEU1047.

(ω) are calculated for further shedding light on the chemical reactivity of the designed molecule. The results in Table 8 revealed that the molecule is soft and potentially active.[27]

The molecular electrostatic potential estimations have been carried out to understand the electronic charge is distributed within compound **15a** and hence the behavior of binding with VEGFER-2 can be predicted. The 3D potential surface map is presented in Fig. 21d. It is noticed that the negative potential areas (red) are localized over oxygen atoms and are ready for electrophilic attacks. Nucleophilic attacks will occur over a positive potential surface that is localized over hydrogen atoms (blue areas). The green zones over the resonance system are ready for hydrophobic interactions.

The total density of states (TDOS) has been carried out and the spectrum is depicted in Fig. 21e. As seen in the TDOS spectrum, the highest density is noticed for vacant orbitals over LUMO.

Topological analysis has been performed using the Multiwfn program to study the quantum theory of atoms in molecules (QTAIM) based on bond bathes, bond critical points (BCP), and QTAIM parameters. AIMALL software was also utilized to calculate the QTAIM parameters such as electron density (ρ), Laplacian ($\nabla^2\rho$), and energy density $H(r)$ as the estimated values are represented in ESI.† while the molecular graph and main generated QTAIM bonding bath with relative critical points are shown in Fig. 21f and g, while the detailed bond critical points (BCP) are resented in ESI.† The calculated (ρ), ($\nabla^2\rho$), and $H(r)$ revealed that the designed drug is stable with internal non-covalent bonding which grants the molecule its stability.

4. Conclusion

In conclusion, this study focused on the design of theobromine derivatives as potential anticancer and VEGFR-2 inhibitors. The

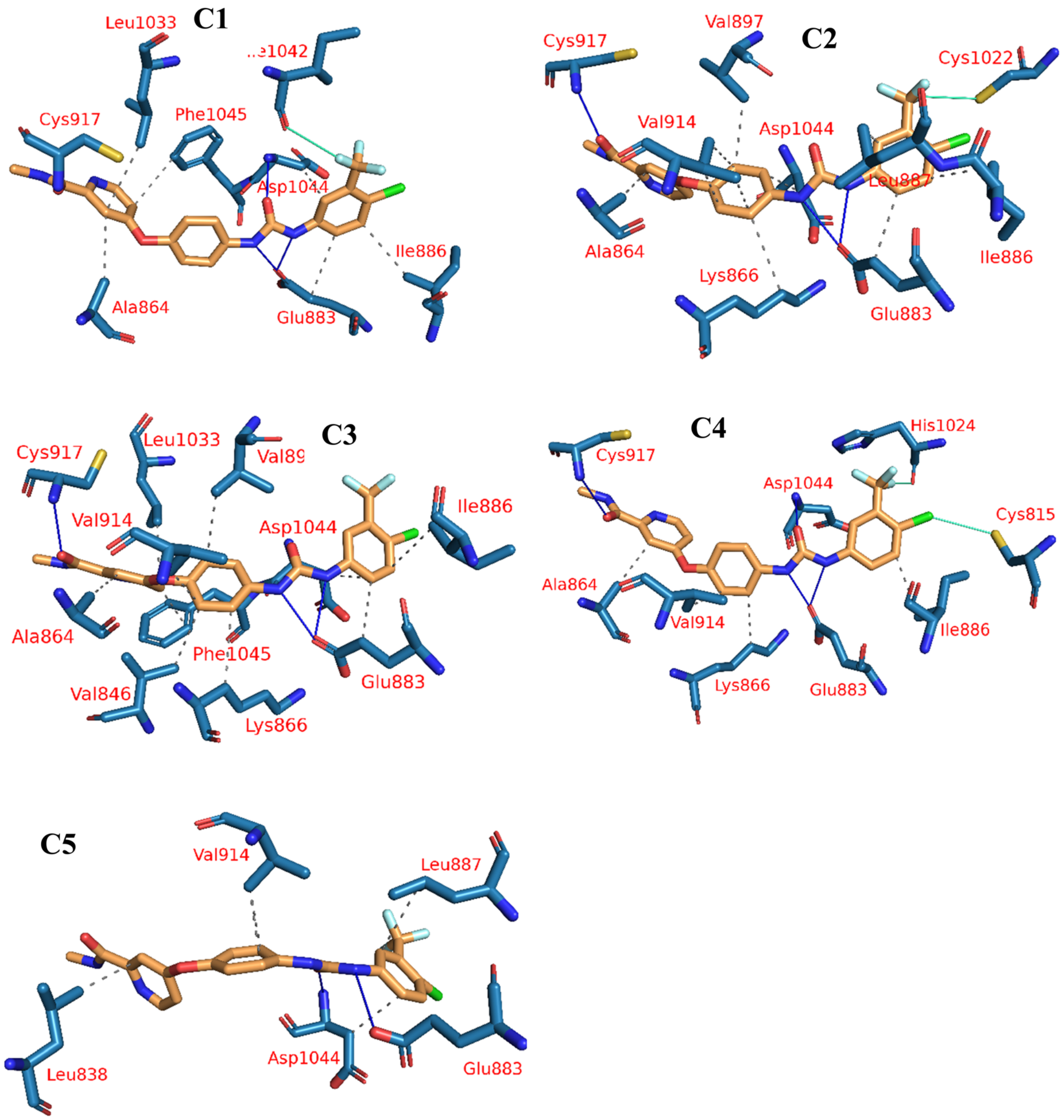

Fig. 15 The five clusters representative obtained from TTClust and their 3D interactions with sorafenib. Grey dashed lines: hydrophobic interactions, blue solid lines: H-bonds, green dashed line: Pi-stacking interaction, cyan solid line: halogen bond, orange sticks: sorafenib, blue sticks: amino acids of VEGFR-2 protein.

investigation involved *in vitro* assessments of the new compounds' effectiveness against MCF-7 and HepG2 cancer cell lines. Compound **15a** emerged as the most cytotoxic member, exhibiting strong inhibitory effects on both HepG2 and MCF-7 cancer cells, with notable selectivity indices. Moreover, compound **15a** demonstrated potent VEGFR-2 inhibitory activity and induced apoptosis in HepG2 cells, as evidenced by increased caspase levels and enhanced apoptotic cell percentages. Furthermore, it significantly hindered the migration and healing abilities of HepG2 cancer cells. Molecular docking MD simulations, PLIP, ED, and DFT studies confirmed the binding affinity of the synthesized compounds to VEGFR-2. Finally, computational ADMET and toxicity assessments supported the potential for drug development of the synthesized compounds. Overall, the combination of biological findings and the CADD methodologies positions compound **15a** as a promising candidate for the development of a novel anti-apoptotic lead anticancer medication.

5. Experimental

5.1. Chemistry

All solvents, reagents, and devices were illustrated in ESI.†

5.1.1. General procedure for the semi-synthesis of compounds 15a,b, 16, and 17. *N*-(4-Acetylphenyl)-2-(3,7-dimethyl-2,6-dioxo-2,3,6,7-tetrahydro-1*H*-purin-1-yl) acetamide **7** (0.001 mol, 0.355 g) and/or *N*-(3-acetylphenyl)-2-(3,7-dimethyl-2,6-dioxo-2,3,6,7-tetrahydro-1*H*-purin-1-yl)acetamide **8** (0.001 mol, 0.355 g) were mixed and refluxed with the appropriate benzohydrazide derivatives **11a–c** and/or **14** (0.001 mol) in absolute ethanol (25 mL) in the

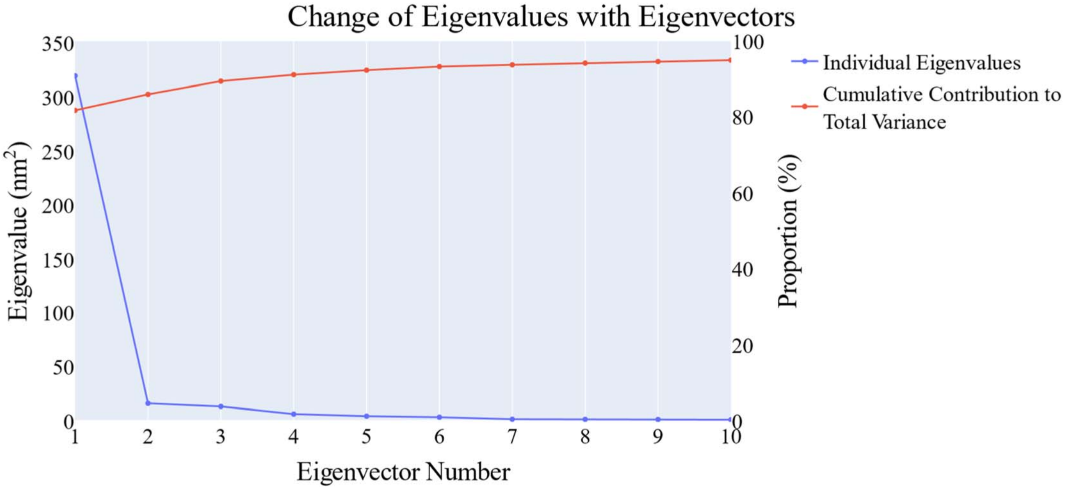

Fig. 16 The change in the eigenvalues with increasing the eigenvectors (blue line) and the cumulative variance retained in the eigenvectors is shown (red line).

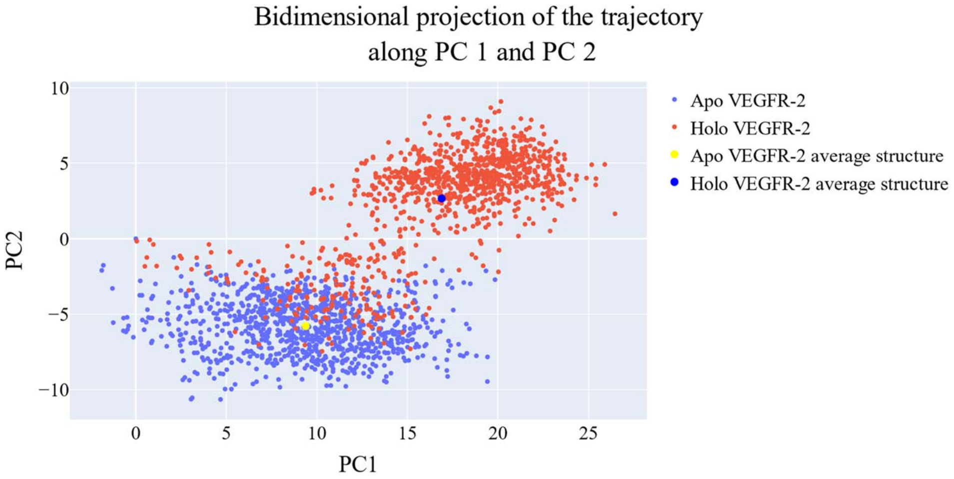

Fig. 17 The projection of each trajectory on the first two eigenvectors.

presence of catalytic amount of glacial acetic acid (3 drops). The mixtures were then concentrated and cooled. The obtained yields were filtered and purified *via* crystallization from methanol to produce the final compounds **15a,b**, **16**, and **17**.

*5.1.1.1. N-(4-(1-(2-(3-Bromobenzoyl)hydrazono)ethyl)phenyl)-2-(3,7-dimethyl-2,6-dioxo-2,3,6,7-tetrahydro-1H-purin-1-yl) acetamide **15a**.* White powder (yield = 0.38 g, 68%); mp = 210–212 °C; IR (KBr) ν cm^{-1}: 3196 (NH), 1704, 1667, 1649 (C=O); ^{1}H NMR (400 MHz, DMSO-d_6) δ 10.93 (s, 1H, NH), 10.45 (s, 1H, NH), 8.08 (d, J = 4.6 Hz, 1H, Ar-H), 7.83 (d, J = 8.5 Hz, 1H, Ar-H), 7.72–7.62 (m, 2H, Ar-H), 7.56–7.43 (m, 3H, Ar-H), 7.39 (m, 2H, Ar-H), 4.71 (s, 2H, CH$_2$), 3.91 (s, 3H, CH$_3$), 3.46 (s, 3H, CH$_3$), 2.29 (s, 3H, CH$_3$); ^{13}C NMR (101 MHz, DMSO-d_6) δ 170.64, 166.41, 164.22, 154.66, 151.37, 148.99, 143.73, 140.45, 139.94, 133.11, 132.35, 130.74, 129.99, 129.05, 128.03, 127.64, 126.93, 120.06, 119.04, 107.07, 43.94, 33.68, 29.93, 14.85; mass (m/z): 554 (M$^+$+2, 8.32%), 552 (M+, 22.99%), 411 (100%, base peak); Anal. calcd for $C_{24}H_{22}BrN_7O_4$ (552.39): C, 52.18; H, 4.01; N, 17.75; found: C, 52.42; H, 4.23; N, 17.98%.

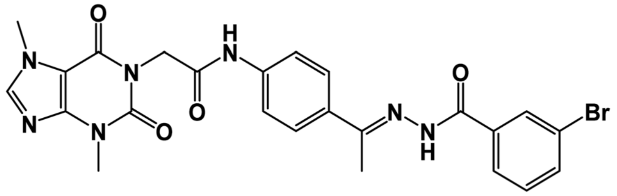

*5.1.1.2. N-(4-(1-(2-(2-Chlorobenzoyl)hydrazono)ethyl)phenyl)-2-(3,7-dimethyl-2,6-dioxo-2,3,6,7-tetrahydro-1H-purin-1-yl) acetamide **15b**.* White powder (yield = 0.38 g, 75%); mp = 207–209 °C; IR (KBr) ν cm^{-1}: 3265 (NH), 1745,1696, 1667 (C=O); ^{1}H NMR (400 MHz, DMSO-d_6) δ 10.92 (s, 1H, NH), 10.43 (s, 1H, NH), 8.03 (d, 1H, Ar-H), 7.84 (d, J = 8.1 Hz, 1H, Ar-H), 7.65 (d, J = 8.1 Hz, 1H, Ar-H), 7.60–7.35 (m, 6H, Ar-H), 4.72 (s, 2H, CH$_2$), 3.91 (s, 3H, CH$_3$), 3.47 (s, 3H, CH$_3$), 2.30 (s, 3H, CH$_3$); ^{13}C NMR (101 MHz, DMSO-d_6) δ 169.98, 166.42, 163.37, 154.67, 151.49, 151.39, 149.01, 143.74, 143.27, 130.96, 130.20, 130.04, 129.28, 129.04, 127.66, 126.93,

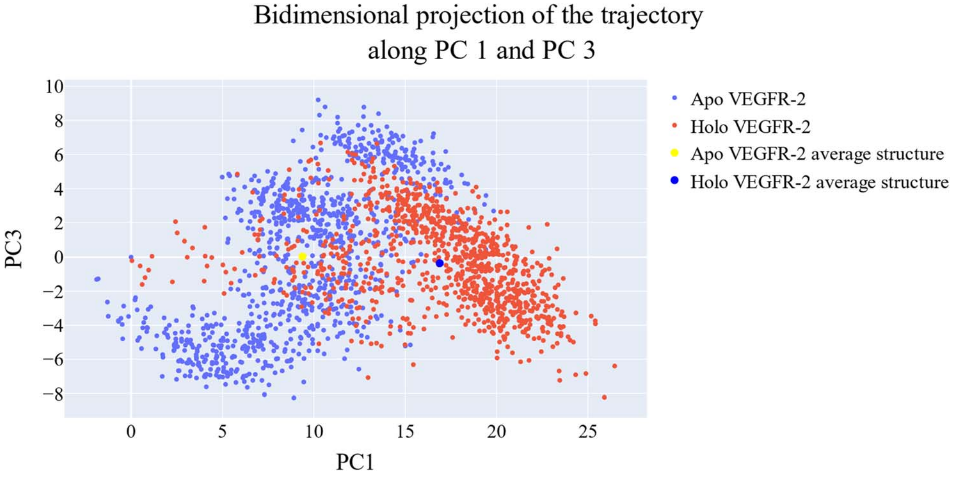

Fig. 18 The projection of each trajectory on the first and third eigenvectors.

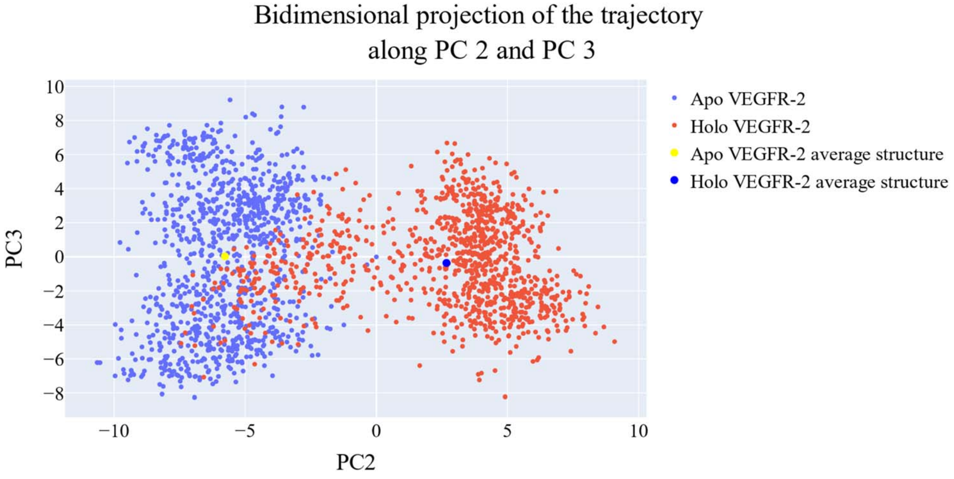

Fig. 19 The projection of each trajectory on the second and third eigenvectors.

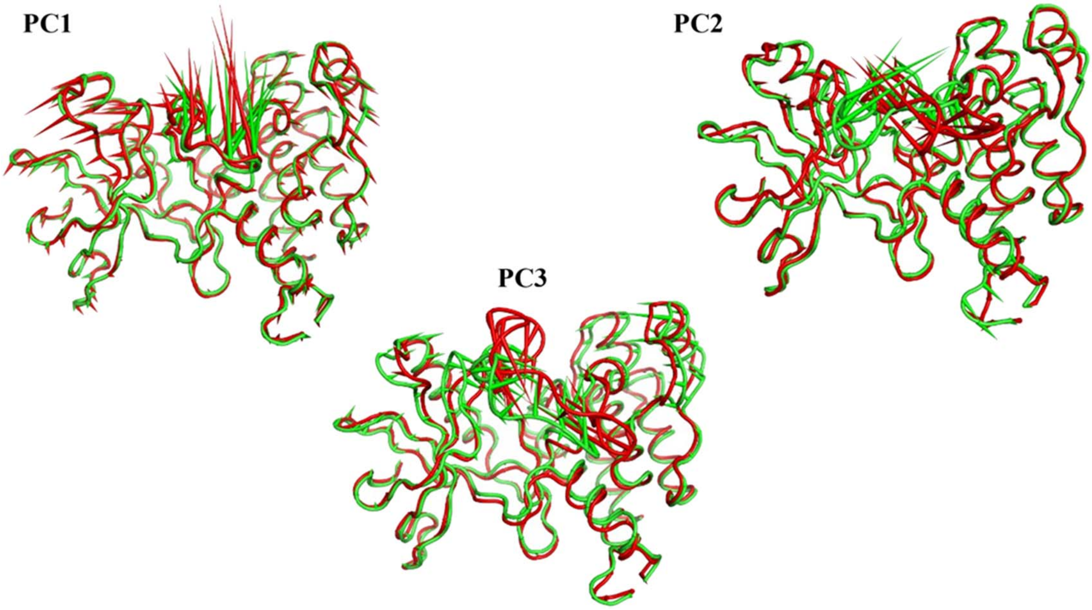

Fig. 20 The porcupine figures of each of the first three eigenvectors for both the apo and VEGFR-2_**15a** systems. Green cartoon: apo protein trajectory, red cartoon: VEGFR-2_**15a** trajectory.

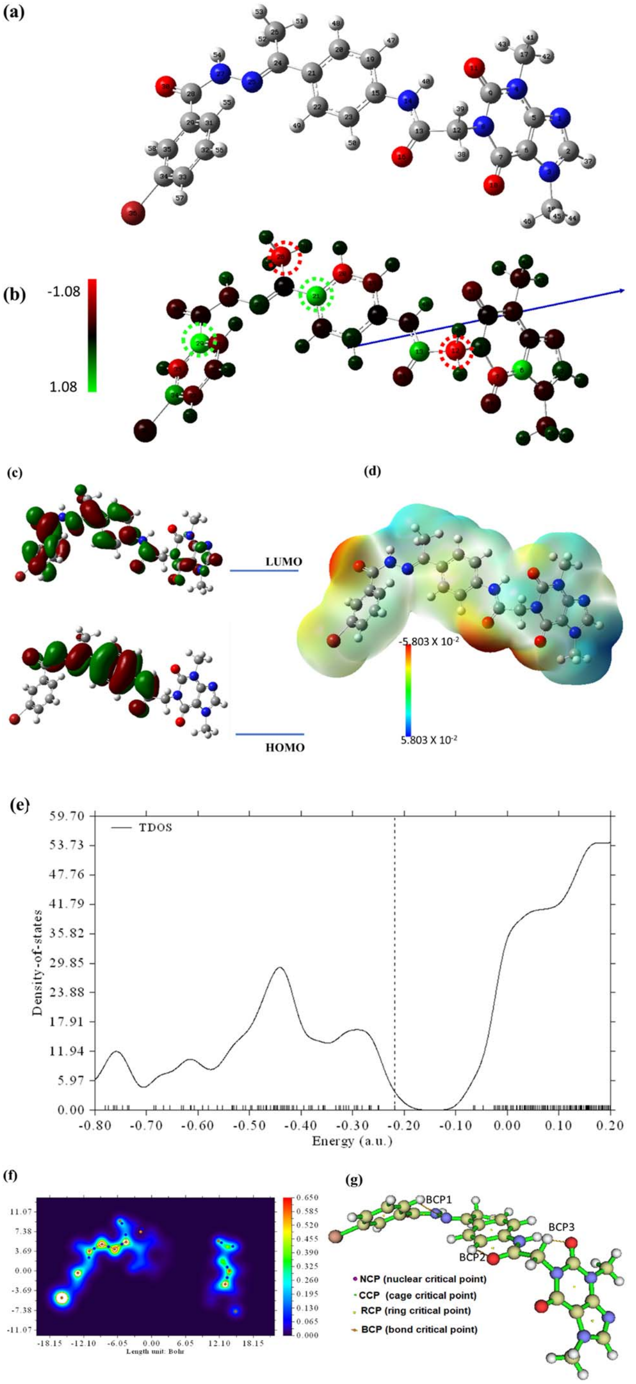

Fig. 21 The optimized geometry (a), the Mullikan atomic charge distribution (b), the frontier molecular orbitals (c), the electrostatic potential (d), the total density of states (e), and the QTAIM maps (f and g) at B3LYB/6-311++G(d,p) for **15a**.

119.07, 107.09, 43.95, 33.68, 29.93, 14.85; Anal. calcd for $C_{24}H_{22}ClN_7O_4$ (507.94): C, 56.75; H, 4.37; N, 19.30; found: C, 56.31; H, 4.10; N, 19.69%.

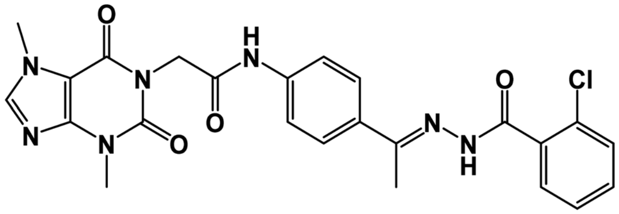

5.1.1.3. *N-(3-(1-(2-(3-Chlorobenzoyl)hydrazono)ethyl)phenyl)-2-(3,7-dimethyl-2,6-dioxo-2,3,6,7-tetrahydro-1H-purin-1-yl) acetamide* ***16***. White powder (yield = 0.39 g, 77%); mp = 200–202 °C; IR (KBr) ν cm^{-1}: 3258 (NH), 1707, 1666 (C═O); ^{1}H NMR (400 MHz, DMSO-d_6) δ 10.89 (s, 1H, NH), 10.44 (s, 1H, NH), 8.32–8.01 (m, 2H, Ar-H), 7.89 (d, 2H, Ar-H), 7.57 (m, 5H, Ar-H), 4.70 (s, 2H, CH_2), 3.89 (s, 3H, CH_3), 3.46 (s, 3H, CH_3), 2.36 (s, 3H, CH_3); ^{13}C NMR (101 MHz, DMSO-d_6) δ 166.41, 154.65, 151.38, 148.96, 143.69, 139.34, 139.03, 136.51, 133.57, 131.78, 130.77, 129.33, 128.11, 127.15, 122.19, 120.71, 117.48, 107.06, 43.89, 33.67, 29.92, 15.22; Anal. calcd for $C_{24}H_{22}ClN_7O_4$ (507.94): C, 56.75; H, 4.37; N, 19.30; Found: C, 56.91; H, 4.52; N, 19.57%.

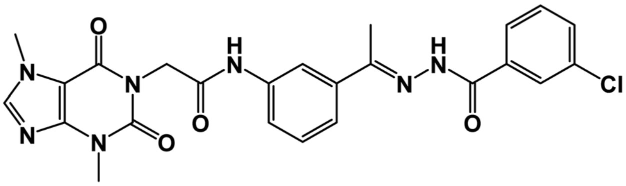

5.1.1.4. *2-(3,7-Dimethyl-2,6-dioxo-2,3,6,7-tetrahydro-1H-purin-1-yl)-N-(4-(1-(2-nicotinoylhydrazono)ethyl)phenyl)acetamide* ***17***. White crystal (yield = 0.31 g, 65%); mp = 230–232 °C; IR (KBr) ν cm^{-1}: 3265 (NH), 1745,1695, 1666 (C═O); ^{1}H NMR (400 MHz, DMSO-d_6) δ 10.91 (s, 1H, NH), 10.42 (s, 1H, NH), 9.04 (s, 1H, Ar-H), 8.75 (s, 1H, Ar-H), 8.15 (d, 2H, Ar-H), 7.91 (d, 2H, Ar-H), 7.60 (d, 3H, Ar-H), 4.71 (s, 2H, CH_2), 3.90 (s, 3H, CH_3), 3.34 (s, 3H, CH_3), 2.36 (s, 3H, CH_3); ^{13}C NMR (101 MHz, DMSO-d_6) δ 166.42, 154.64, 151.36, 148.98, 143.74, 143.26, 133.21, 127.71, 123.92, 119.07, 107.06, 43.94, 33.69, 29.93, 14.95; Anal. calcd. for $C_{23}H_{22}N_8O_4$ (474.48): C, 58.22; H, 4.67; N, 23.62; Found: C, 58.59; H, 4.42; N, 23.91%.

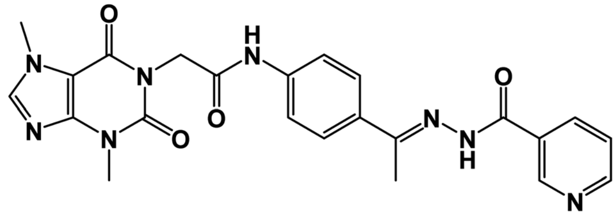

5.2. Biological examinations

5.2.1. *In vitro* anti-proliferative activity. To assess the inhibitory potential of the synthesized theobromine derivatives

Table 8 The DFT calculated global reactivity parameters for **15a**

IP	EA	μ (eV)	χ (eV)	η (eV)	σ (eV)	ω (eV)	D_m (Debye)	TE (eV)	ΔN_{max}	ΔE (eV)
5.953	−1.783	−2.085	2.085	3.868	0.259	8.406	11.596	−113923.2	0.539	−8.406

15a, **15b**, **16** and **17** against the proliferation of MCF-7 and HepG2 cancer cells an *in vitro* MTT assay was applied.[28] The research's ESI† file goes into more insight into this experiment.

5.2.2. *In vitro* VEGFR-2 inhibition. The synthesized theobromine derivatives **15a**, **15b**, **16** and **17** were subjected to an *in vitro* evaluation against VEGFR-2 *via* the implementation of a VEGFR-2 ELISA kit.[29] The research's ESI† file goes into more insight into this experiment.

5.2.3. Flow cytometry assay. The potential inhibition of compound **15a** on HepG2 apoptosis was evaluated using flow cytometry.[30] The research's ESI† file goes into more insight into this experiment.

5.2.4. Caspase 3 and 9 determinations. The potential inhibition of compound **15a** on caspases level in HepG2 cells was evaluated using RT PCR analysis. The research's ESI† file goes into more insight into this experiment.

5.3. *In silico* studies

5.3.1. Docking studies. Utilizing docking investigations with MOE2019 software, the potential inhibitory effects of the synthesized theobromine derivatives **15a**, **15b**, **16** and **17** against VEGFR-2 [PDB ID: 2OH4, resolution: 2.05] were assessed. The research's ESI† file goes into more insight into this experiment.[31–33]

5.3.2. ADMET studies. ADMET profiles of the synthesized theobromine derivatives **15a**, **15b**, **16** and **17** were evaluated computationally by Discovery Studio 4.0. The research's ESI† file goes into more insight into this experiment.[34,35]

5.3.3. Toxicity studies. The toxicity profiles of the synthesized theobromine derivatives **15a**, **15b**, **16** and **17** were evaluated computationally by Discovery Studio 4.0. The research's ESI† file goes into more insight into this experiment.[36–38]

5.3.4. MD simulations. Compound **15a**'s capacity to inhibit the VEGFR-2 was examined computationally through MD simulations that were run by the CHARMM-GUI web server[39] and the MD engine GROMACS 2021.[40,41] The research's ESI† file goes into more insight into this experiment.

5.3.5. MM-GBSA analysis. MM-GBSA analysis of the VEGFR-2-compound **15a** complex was evaluated by the Gmx_MMPBSA package.[42,43] The research's ESI† file goes into more insight into this experiment.

5.3.6. ProLIF analysis. ProLIF analysis of VEGFR-2-**15a** complex was evaluated by the GROMACS package.[44–46] The research's ESI† file goes into more insight into this experiment.

5.3.7. Essential dynamics (ED) analysis. Essential Dynamics (ED) analysis of VEGFR-2-**15a** complex was evaluated by GROMACS by utilizing the gmx covar command.[47] The research's ESI† file goes into more insight into this experiment.

5.3.8. Cosine Content analysis. Cosine Content analysis of VEGFR-2-**15a** complex was evaluated by GROMACS.[48] The research's ESI† file goes into more insight into this experiment.

5.3.9. Bidimensional Projections analysis. Bidimensional Projections analysis of the VEGFR-2-**15a** complex was evaluated by GROMACS[49,50] The research's ESI† file goes into more insight into this experiment.

5.3.10. Density function theory (DFT) calculations. DFT analyses were evaluated for **15a** by Gaussian software. The research's ESI† file goes into more insight into this experiment.[51,52]

Conflicts of interest

There are no conflicts of interest to declare.

Acknowledgements

This research was funded by Princess Nourah bint Abdulrahman University Researchers Supporting Project number (PNURSP2023R116), Princess Nourah bint Abdulrahman University, Riyadh, Saudi Arabia. The authors extend their appreciation to the Research Center at AlMaarefa University for funding this work.

References

1 F. Bray, J. Ferlay, I. Soerjomataram, R. L. Siegel, L. A. Torre and A. Jemal, Global cancer statistics 2018: GLOBOCAN estimates of incidence and mortality worldwide for 36 cancers in 185 countries, *CA Cancer J Clin*, 2018, **68**(6), 394–424.

2 A. Belal, N. M. Abdel Gawad, A. B. Mehany, M. A. Abourehab, H. Elkady, A. A. Al-Karmalawy and A. S. Ismael, Design, synthesis and molecular docking of new fused 1 H-pyrroles, pyrrolo [3,2-*d*] pyrimidines and pyrrolo [3,2-*e*][1,4] diazepine derivatives as potent EGFR/CDK2 inhibitors, *J. Enzyme Inhib. Med. Chem.*, 2022, **37**(1), 1884–1902.

3 M. M. Khalifa, A. A. Al-Karmalawy, E. B. Elkaeed, M. S. Nafie, M. A. Tantawy, I. H. Eissa and H. A. Mahdy, Topo II inhibition and DNA intercalation by new phthalazine-based derivatives as potent anticancer agents: design, synthesis, anti-proliferative, docking, and *in vivo* studies, *J. Enzyme Inhib. Med. Chem.*, 2022, **37**(1), 299–314.

4 V. T. DeVita Jr and E. Chu, A history of cancer chemotherapy, *Cancer Res.*, 2008, **68**(21), 8643–8653.

5 I. J. Fidler and L. M. Ellis, Chemotherapeutic drugs—more really is not better, *Nat. Med.*, 2000, **6**(5), 500–502.

6 A. A. Shah, M. A. Kamal and S. Akhtar, Tumor angiogenesis and VEGFR-2: mechanism, pathways and current biological therapeutic interventions, *Curr. Drug Metab.*, 2021, **22**(1), 50–59.

7 E. Z. Elrazaz, R. A. Serya, N. S. Ismail, A. Albohy, D. A. Abou El Ella and K. A. Abouzid, Discovery of potent thieno [2,3-*d*] pyrimidine VEGFR-2 inhibitors: Design, synthesis and enzyme inhibitory evaluation supported by molecular dynamics simulations, *Bioorg. Chem.*, 2021, **113**, 105019.

8 A. M. Metwaly, Z. Lianlian, H. Luqi and D. Deqiang, Black ginseng and its saponins: Preparation, phytochemistry and pharmacological effects, *Molecules*, 2019, **24**(10), 1856.

9 A. M. Metwaly, M. M. Ghoneim, I. H. Eissa, I. A. Elsehemy, A. E. Mostafa, M. M. Hegazy, W. M. Afifi and D. Dou, Traditional ancient Egyptian medicine: A review, *Saudi J. Biol. Sci.*, 2021, **28**(10), 5823–5832.

10 D. J. Newman and G. M. Cragg, Natural products as sources of new drugs from 1981 to 2014, *J. Nat. Prod.*, 2016, **79**(3), 629–661.

11 R. da Rosa, E. P. Schenkel and L. S. C. Bernardes, Semisynthetic and newly designed derivatives based on natural chemical scaffolds: moving beyond natural products to fight Trypanosoma cruzi, *Phytochem. Rev.*, 2020, **19**(1), 105–122.

12 A. Sánchez-Recillas, G. Navarrete-Vázquez, S. Hidalgo-Figueroa, M. Y. Rios, M. Ibarra-Barajas and S. Estrada-Soto, Semisynthesis, ex vivo evaluation, and SAR studies of coumarin derivatives as potential antiasthmatic drugs, *Eur. J. Med. Chem.*, 2014, **77**, 400–408.

13 F. Carla Cadoná, A. Kolinski Machado, V. Farina Azzolin, F. Barbisan, E. Bortoluzzi Dornelles, W. Glanzner, P. D. Bayard Gonçalves, C. Elias Assmann, E. Esteves Ribeiro and I. Beatrice Mânica da Cruz, Guaraná a caffeine-rich food increases oxaliplatin sensitivity of colorectal HT-29 cells by apoptosis pathway modulation, *Anti-Cancer Agents Med. Chem.*, 2016, **16**(8), 1055–1065.

14 N. Sugimoto, S. Miwa, M. Katakura, K. Matsuzaki, O. Shido, H. Tsuchiya and A. Yachie, Theobromine, the primary methylxanthine found in Theobroma cacao, inhibits malignant glioblastoma cell growth by negatively regulating Akt/mammalian target of rapamycin kinase (LB836), *FASEB J.*, 2014, **28**, LB836.

15 E. Barcz, E. Sommer, I. Sokolnicka, K. Gawrychowski, K. Roszkowska-Purska, P. Janik and E. Skopinska-Rózewska, The influence of theobromine on angiogenic activity and proangiogenic cytokines production of human ovarian cancer cells, *Oncol. Rep.*, 1998, **5**(2), 517–537.

16 M. Gil, E. Skopińska-Rózewska, D. Radomska, U. Demkow, H. Skurzak, M. Rochowska, J. Beuth and K. Roszkowski, Effect of purinergic receptor antagonists suramin and theobromine on tumor-induced angiogenesis in BALB/c mice, *Folia Biol.*, 1993, **39**(2), 63–68.

17 M. M. Alanazi, H. A. Mahdy, N. A. Alsaif, A. J. Obaidullah, H. M. Alkahtani, A. A. Al-Mehizia, S. M. Alsubaie, M. A. Dahab and I. H. Eissa, New bis ([1,2,4]triazolo)[4,3-*a*:3′,4′-*c*] quinoxaline derivatives as VEGFR-2 inhibitors and apoptosis inducers: Design, synthesis, *in silico* studies, and anticancer evaluation, *Bioorg. Chem.*, 2021, **112**, 104949.

18 M. M. Alanazi, H. Elkady, N. A. Alsaif, A. J. Obaidullah, H. M. Alkahtani, M. M. Alanazi, M. A. Alharbi, I. H. Eissa and M. A. Dahab, New quinoxaline-based VEGFR-2 inhibitors: design, synthesis, and antiproliferative evaluation with *in silico* docking, ADMET, toxicity, and DFT studies, *RSC Adv.*, 2021, **11**(48), 30315–30328.

19 R. G. Yousef, H. M. Sakr, I. H. Eissa, A. B. Mehany, A. M. Metwaly, M. A. Elhendawy, M. M. Radwan, M. A. ElSohly, H. S. Abulkhair and K. El-Adl, New quinoxaline-2 (1 H)-ones as potential VEGFR-2 inhibitors: Design, synthesis, molecular docking, ADMET profile and anti-proliferative evaluations, *New J. Chem.*, 2021, **45**(36), 16949–16964.

20 L. Adnane, P. A. Trail, I. Taylor and S. M. Wilhelm, Sorafenib (BAY 43-9006, Nexavar®), a dual-action inhibitor that targets RAF/MEK/ERK pathway in tumor cells and tyrosine kinases VEGFR/PDGFR in tumor vasculature, *Methods Enzymol.*, 2006, **407**, 597–612.

21 F.-W. Peng, D.-K. Liu, Q.-W. Zhang, Y.-G. Xu and L. Shi, VEGFR-2 inhibitors and the therapeutic applications thereof: a patent review (2012-2016), *Expert Opin. Ther. Pat.*, 2017, **27**(9), 987–1004.

22 R. G. Yousef, A. Elwan, I. M. Gobaara, A. B. Mehany, W. M. Eldehna, S. A. El-Metwally, B. A. Alsfouk, E. B. Elkaeed, A. M. Metwaly and I. H. Eissa, Anti-cancer and immunomodulatory evaluation of new nicotinamide derivatives as potential VEGFR-2 inhibitors and apoptosis inducers: *in vitro* and *in silico* studies, *J. Enzyme Inhib. Med. Chem.*, 2022, **37**(1), 2206–2222.

23 R. G. Yousef, A. Ibrahim, M. M. Khalifa, W. M. Eldehna, I. M. Gobaara, A. B. Mehany, E. B. Elkaeed, A. A. Alsfouk, A. M. Metwaly and I. H. Eissa, Discovery of new nicotinamides as apoptotic VEGFR-2 inhibitors: Virtual screening, synthesis, anti-proliferative, immunomodulatory, ADMET, toxicity, and molecular dynamic simulation studies, *J. Enzyme Inhib. Med. Chem.*, 2022, **37**(1), 1389–1403.

24 R. G. Yousef, H. Elkady, E. B. Elkaeed, I. M. Gobaara, H. A. Al-Ghulikah, D. Z. Husein, I. M. Ibrahim, A. M. Metwaly and I. H. Eissa, (*E*)-*N*-(3-(1-(2-(4-(2,2,2-Trifluoroacetamido) benzoyl) hydrazono) ethyl) phenyl) nicotinamide: A Novel Pyridine Derivative for Inhibiting Vascular Endothelial Growth Factor Receptor-2: Synthesis, Computational, and Anticancer Studies, *Molecules*, 2022, **27**(22), 7719.

25 T. Hou, L. Zhu, L. Chen and X. Xu, Mapping the binding site of a large set of quinazoline type EGF-R inhibitors using molecular field analyses and molecular docking studies, *J. Chem. Inf. Comput. Sci.*, 2003, **43**(1), 273–287.

26 D. Z. Husein, R. Hassanien and M. Khamis, Cadmium oxide nanoparticles/graphene composite: Synthesis, theoretical insights into reactivity and adsorption study, *RSC Adv.*, 2021, **11**(43), 27027–27041.

27 T. Wang and D. Z. Husein, Novel synthesis of multicomponent porous nano-hybrid composite, theoretical investigation using DFT and dye adsorption applications: Disposing of waste with waste, *Environ. Sci. Pollut. Res.*, 2023, **30**(4), 8928–8955.

28 A. Van de Loosdrecht, R. Beelen, G. Ossenkoppele, M. Broekhoven and M. Langenhuijsen, A tetrazolium-based colorimetric MTT assay to quantitate human monocyte mediated cytotoxicity against leukemic cells from cell lines and patients with acute myeloid leukemia, *J. Immunol. Methods*, 1994, **174**(1–2), 311–320.

29 E. B. Elkaeed, R. G. Yousef, H. Elkady, A. B. Mehany, B. A. Alsfouk, D. Z. Husein, I. M. Ibrahim, A. M. Metwaly and I. H. Eissa, *In silico*, *in vitro* VEGFR-2 inhibition, and anticancer activity of a 3-(hydrazonomethyl) naphthalene-2-ol derivative, *J. Biomol. Struct. Dyn.*, 2022, 1–16.

30 W. M. Eldehna, M. A. El Hassab, Z. M. Elsayed, T. Al-Warhi, H. Elkady, M. F. Abo-Ashour, M. A. Abourehab, I. H. Eissa and H. A. Abdel-Aziz, Design, synthesis, *in vitro* biological assessment and molecular modeling insights for novel 3-

(naphthalen-1-yl)-4,5-dihydropyrazoles as anticancer agents with potential EGFR inhibitory activity, *Sci. Rep.*, 2022, **12**(1), 12821.

31 M. S. Taghour, H. Elkady, W. M. Eldehna, N. M. El-Deeb, A. M. Kenawy, E. B. Elkaeed, A. A. Alsfouk, M. S. Alesawy, A. M. Metwaly and I. H. Eissa, Design and synthesis of thiazolidine-2,4-diones hybrids with 1,2-dihydroquinolones and 2-oxindoles as potential VEGFR-2 inhibitors: In-vitro anticancer evaluation and in-silico studies, *J. Enzyme Inhib. Med. Chem.*, 2022, **37**(1), 1903–1917.

32 E. B. Elkaeed, R. G. Yousef, H. Elkady, I. M. Gobaara, A. A. Alsfouk, D. Z. Husein, I. M. Ibrahim, A. M. Metwaly and I. H. Eissa, The assessment of anticancer and VEGFR-2 inhibitory activities of a new 1 H-indole derivative: *In silico* and *in vitro* approaches, *Processes*, 2022, **10**(7), 1391.

33 C. Ma, M. S. Taghour, A. Belal, A. B. Mehany, N. Mostafa, A. Nabeeh, I. H. Eissa and A. A. Al-Karmalawy, Design and synthesis of new quinoxaline derivatives as potential histone deacetylase inhibitors targeting hepatocellular carcinoma: *in silico*, *in vitro*, and SAR studies, *Front. Chem.*, 2021, **9**, 725135.

34 E. B. Elkaeed, R. G. Yousef, M. M. Khalifa, A. Ibrahim, A. B. Mehany, I. M. Gobaara, B. A. Alsfouk, W. M. Eldehna, A. M. Metwaly and I. H. Eissa, Discovery of New VEGFR-2 Inhibitors: Design, Synthesis, Anti-Proliferative Evaluation, Docking, and MD Simulation Studies, *Molecules*, 2022, **27**(19), 6203.

35 M. S. Alesawy, A. E. Abdallah, M. S. Taghour, E. B. Elkaeed, I. H. Eissa and A. M. Metwaly, In silico studies of some isoflavonoids as potential candidates against COVID-19 targeting human ACE2 (hACE2) and viral main protease (Mpro), *Molecules*, 2021, **26**(9), 2806.

36 H. Elkady, A. Elwan, H. A. El-Mahdy, A. S. Doghish, A. Ismail, M. S. Taghour, E. B. Elkaeed, I. H. Eissa, M. A. Dahab and H. A. Mahdy, New benzoxazole derivatives as potential VEGFR-2 inhibitors and apoptosis inducers: Design, synthesis, anti-proliferative evaluation, flowcytometric analysis, and *in silico* studies, *J. Enzyme Inhib. Med. Chem.*, 2022, **37**(1), 403–416.

37 I. H. Eissa, M. M. Khalifa, E. B. Elkaeed, E. E. Hafez, A. A. Alsfouk and A. M. Metwaly, *In silico* exploration of potential natural inhibitors against SARS-CoV-2 nsp10, *Molecules*, 2021, **26**(20), 6151.

38 I. H. Eissa, M. A. Dahab, M. K. Ibrahim, N. A. Alsaif, A. Alanazi, S. I. Eissa, A. B. Mehany and A. M. Beauchemin, Design and discovery of new antiproliferative 1,2,4-triazin-3 (2H)-ones as tubulin polymerization inhibitors targeting colchicine binding site, *Bioorg. Chem.*, 2021, **112**, 104965.

39 M. J. Abraham, T. Murtola, R. Schulz, S. Páll, J. C. Smith, B. Hess and E. Lindahl, GROMACS: High performance molecular simulations through multi-level parallelism from laptops to supercomputers, *SoftwareX*, 2015, **1**, 19–25.

40 S. Jo, X. Cheng, S. M. Islam, L. Huang, H. Rui, A. Zhu, H. S. Lee, Y. Qi, W. Han and K. Vanommeslaeghe, CHARMM-GUI PDB manipulator for advanced modeling and simulations of proteins containing nonstandard residues, *Adv. Protein Chem. Struct. Biol.*, 2014, **96**, 235–265.

41 J. Lee, X. Cheng, S. Jo, A. D. MacKerell, J. B. Klauda and W. Im, CHARMM-GUI input generator for NAMD, GROMACS, AMBER, OpenMM, and CHARMM/OpenMM simulations using the CHARMM36 additive force field, *Biophys. J.*, 2016, **110**(3), 641a.

42 T. Tuccinardi, What is the current value of MM/PBSA and MM/GBSA methods in drug discovery?, *Expert Opin. Drug Discovery*, 2021, **16**(11), 1233–1237.

43 M. S. Valdés-Tresanco, M. E. Valdés-Tresanco, P. A. Valiente and E. Moreno, gmx_MMPBSA: a new tool to perform end-state free energy calculations with GROMACS, *J. Chem. Theory Comput.*, 2021, **17**(10), 6281–6291.

44 C. Bouysset and S. Fiorucci, ProLIF: a library to encode molecular interactions as fingerprints, *J. Cheminf.*, 2021, **13**, 1–9.

45 S. Salentin, S. Schreiber, V. J. Haupt, M. F. Adasme and M. Schroeder, PLIP: fully automated protein–ligand interaction profiler, *Nucleic Acids Res.*, 2015, **43**(W1), W443–W447.

46 T. Tubiana, J.-C. Carvaillo, Y. Boulard and S. Bressanelli, TTClust: a versatile molecular simulation trajectory clustering program with graphical summaries, *J. Chem. Inf. Model.*, 2018, **58**(11), 2178–2182.

47 A. Amadei, A. B. Linssen and H. J. Berendsen, Essential dynamics of proteins, *Proteins: Struct., Funct., Bioinf.*, 1993, **17**(4), 412–425.

48 E. Papaleo, P. Mereghetti, P. Fantucci, R. Grandori and L. De Gioia, Free-energy landscape, principal component analysis, and structural clustering to identify representative conformations from molecular dynamics simulations: the myoglobin case, *J. Mol. Graphics Modell.*, 2009, **27**(8), 889–899.

49 G. G. Maisuradze and D. M. Leitner, Free energy landscape of a biomolecule in dihedral principal component space: Sampling convergence and correspondence between structures and minima, *Proteins: Struct., Funct., Bioinf.*, 2007, **67**(3), 569–578.

50 B. Hess, Similarities between principal components of protein dynamics and random diffusion, *Phys. Rev. E: Stat. Phys., Plasmas, Fluids, Relat. Interdiscip. Top.*, 2000, **62**(6), 8438.

51 E. B. Elkaeed, R. G. Yousef, H. Elkady, I. M. Gobaara, B. A. Alsfouk, D. Z. Husein, I. M. Ibrahim, A. M. Metwaly and I. H. Eissa, Design, synthesis, docking, DFT, MD simulation studies of a new nicotinamide-based derivative: *In vitro* anticancer and VEGFR-2 inhibitory effects, *Molecules*, 2022, **27**(14), 4606.

52 E. B. Elkaeed, I. H. Eissa, H. Elkady, A. Abdelalim, A. M. Alqaisi, A. A. Alsfouk, A. Elwan and A. M. Metwaly, A multistage *in silico* study of natural potential inhibitors targeting SARS-CoV-2 main protease, *Int. J. Mol. Sci.*, 2022, **23**(15), 8407.